"This is the peer reviewed version of the following article: Bradac, C., Lim, S. F., Chang, H.-C., Aharonovich, I., Optical Nanoscale Thermometry: From Fundamental Mechanisms to Emerging Practical Applications. Adv. Optical Mater. 2020, 2000183., which has been published in final form at https://doi.org/10.1002/adom.202000183. This article may be used for non-commercial purposes in accordance with Wiley Terms and Conditions for Self-Archiving

ADVANCED OPTICAL MATERIALS

www.advopticalmat.de

Optical Nanoscale Thermometry: From Fundamental Mechanisms to Emerging Practical Applications

Q1 *Carlo Bradac,* Shuang Fang Lim, Huan-Cheng Chang, and Igor Aharonovich*

Knowledge of temperature and temperature gradients with nanoscale resolution is critical for a variety of applications in medicine, nanoelectronics, biology, and solid-state-based devices. The number of existing nanothermometry techniques is remarkably large, varying for materials, mechanisms, sensitivity, and operating ranges. In this work, a selected group of prominent nanoscale thermosensors is reviewed, which are all-optical and nanoparticle-based. Specifically, the focus is on the analysis of their fundamental mechanism to identify absolute, intrinsic capabilities and limitations of each nanothermometry platform. Prominent applications as well as future challenges and opportunities in the field are discussed.

1. Introduction

Nanothermometry is the ability to measure—and potentially control—temperature at the nanoscale and it has become a topic of fervent research. The interest emerges from a combination of factors, which are being developed organically and feed off one another. Advancements in material science are making available nanomaterials, which can probe the nanoscale regime while displaying physicochemical properties highly sensitive to temperature variations. Simultaneously, the steady development of a wide range of nanotechnologies[1]—e.g., in nanophotonics, nanoelectronics, nanofluidics, and nanomedicine—calls for the capability to monitor processes, objects, and devices, which occur and operate at nanometric scales, and can be strongly affected by local temperature changes. The prospect to develop disruptive thermometry-based nanoapplications is playing a key role too. Realistic proposals range from thermally driven gene expression[2,3] to tumor metabolism control[4] and targeted therapy,[5,6] as well as temperature management in nanoscale high-power electronics.[1]

These factors have led to the advancement of a widespread collection of nanothermometry techniques based on various materials, exploiting different mechanisms and optimized to operate at specific regimes or temperature ranges. Nanoscale thermometry is the subject of several review articles.[7–11] This work differentiates itself from the existing literature due to its focus. Many reviews present a selection of nanoscale thermometry techniques with emphasis on their phenomenological description and their known applications. We instead focus on the in-depth analysis of their fundamental mechanisms. Our aim is to identify the absolute, intrinsic strengths and limits—both fundamental and practical—of each selected technique within a clear classification and benchmarking framework. We also present and discuss selected applications where nanoscale thermometry shows potential for significant impact and we highlight outstanding challenges and open opportunities in the field.

2. Classification and Benchmarking

The range of available nanothermometry techniques is remarkably large, varying in material, underlying mechanism, and specific applicability. Given the stated focus of this review, we ought to define the framework within which the selected techniques are evaluated. The various methods are classified in type and scope and are benchmarked based on a few key performance factors, which include sensitivity, resolution, range, and utility.

2.1. Classes of Thermometers

Micro- and nanothermometry techniques can be categorized following various criteria. This usually matters for the purpose of comparing directly limits and performance of different methods within each class.

2.1.1. Primary (Absolute) versus Secondary (Calibrated) Thermometers

The first major criterion for categorizing different nanothermometry techniques is fundamental. Thermometers are classified

---

C. Bradac, I. Aharonovich
School of Mathematical and Physical Sciences
Faculty of Science
University of Technology Sydney
Q2 Ultimo, NSW 2007, Australia
Q3 E-mail: carlo.bradac@uts.edu.au
Q4 S. F. Lim
Department of Physics
Q5 North Carolina State University
Raleigh, NC 27695, USA
H.-C. Chang
Institute of Atomic and Molecular Sciences
Academia Sinica
Taipei 106, Taiwan
I. Aharonovich
Centre of Excellence for Transformative Meta-Optical Systems
University of Technology Sydney
Ultimo, NSW 2007, Australia

The ORCID identification number(s) for the author(s) of this article can be found under https://doi.org/10.1002/adom.202000183.

DOI: 10.1002/adom.202000183

as primary or secondary on the basis of the underlying thermodynamic laws, principle, and quantities used to determine the temperature.[12]

Primary thermometers are based on state equations where temperature is a state variable and it is therefore determined in an absolute manner. Typical examples include the equations for ideal gases, the speed of sound in a gas, the Johnson–Nyquist (thermal) noise in an electrical resistor, etc. In all these cases, there is an equation, $f(T, q_1, q_2, \ldots, q_n) = 0$, which allows the absolute derivation of the temperature T from knowing the other quantities q_i. Primary thermometers are often inconvenient from a practical standpoint due to low reproducibility, slow response time, and lack of ease of operation.[13]

Secondary thermometers are relative. Knowledge of the measured quantity is not sufficient to derive directly the temperature; they instead require calibration against a reference system. In secondary thermometers, changes in temperature produce corresponding variations to an observable, O, but the dependence $O(T)$ needs to be determined using known reference values, for instance fixed points such as triple points of gases and liquids or melting points of metals, which occur reproducibly at the same temperature and have been agreed upon in the International Temperature Scale (ITS-90).[14] While obvious, this aspect is crucial as the calibration process can be nontrivial. For instance, some secondary nanothermometers rely on mapping temperature changes directly onto variations in photoluminescence (PL) intensity. If the precalibrated nanothermometer is used in an environment, which absorbs or scatters light at the sensor's operating wavelengths, the resulting temperature reading could be inaccurate. This is, in fact, one of the most critical limitations of many proposed all-optical nanothermometry techniques. Nevertheless, in general secondary (nano)thermometers are highly reproducible, have a fast readout and can be used flexibly in a wide range of applications. Most of the nanothermometers discussed in this review belong to the class of secondary thermometers.

2.1.2. Nature of the Signal

Thermometry techniques can also be classified based on the type of signal they utilize to map temperature—e.g., electric, magnetic, optical, etc. This matters for utility reasons (cf. Section 2.2.5), meaning that the nature of the measurement might determine whether the technique is compatible with specific applications. For instance, an all-optical technique is likely less-invasive than one requiring the reading of an electrical signal, making it more suitable for uses such as measuring temperature inside a living cell. In this work we focus mainly on thermosensing methods based on optical measurements.

2.1.3. Sensor versus Sensorless Techniques

The distinction in this case is between methods that rely on a physical sensor in contact with the object to be sensed (e.g., nanoparticle-based thermometers) and those where the temperature reading is done remotely or contactless (e.g., an infrared (IR) thermometer or pyrometer). For contact-sensors, this classification is relevant to determine the utility of the technique (cf. Section 2.2.5), for it might impose limits on its use in certain contexts. For instance, a nanoparticle-based thermometer might not be suitable for measuring the temperature inside a cell if the nanoparticle itself is cytotoxic.

Carlo Bradac is Research Fellow at the University of Technology, Sydney (Australia). He received his Bachelor (2004) and Master degrees (2006) in Engineering for Physics and Mathematics at the Polytechnic of Milan (Italy). He worked as Application Engineer (2006–2007) and as Process, Control & Automation Engineer (2007–2008). He received his Ph.D. in Physics at Macquarie University (Sydney, Australia) in 2012, and worked as Research Fellow at Sydney University (2012–2013), Macquarie University (2013–2017), and the University of Technology of Sydney (2017–present). His research focuses on solid-state quantum optics, photonics, and biomedicine.

2.2. Benchmarking

Having a large range of nanothermometry techniques available means that there is an equivalently large spread of performance and applicability.

2.2.1. Spatial Resolution

Defining the spatial resolution of a thermometry technique is nontrivial at the nanoscale.[15,16] In this regime, the sensor-plus-object system might consist of just a small number of fundamental constituents (e.g., atoms). The granularity of the sensed object becomes important. As a (large quantum) system is subdivided into smaller and smaller subdomains, there might be a limit to what is the smallest grain for which the concept of temperature distribution holds. The size of the sensor, how it compares with that of said grains and how localized is the sensor–object interaction also matter. Intuitively, it is desirable for the sensor to be smaller—for this should give the sensor sufficiently high resolution and low thermal load to measure the temperature of the object's subdomains without, simultaneously, affecting their temperature. Heat transfer also becomes nontrivial at the nanoscale. The Fourier heat conduction theory is valid only when there are enough scattering events such that the heat carriers (electrons or phonons) can exchange energy with the surrounding medium. When the size of the system—object and/or sensor—is much smaller than the mean free path (MFP) of the heat-carriers, very few scattering events can occur and the heat transport becomes nondiffusive as the carriers move ballistically without collisions.[17–19] Furthermore, as heat-carriers have a distribution of MFPs, from nanometers to hundreds of micrometers,[20] there is a complex spectrum of behaviors: from fully diffusive for carriers with MFPs shorter than the size of the heat source to ballistic for those with longer MFPs, and quasi-ballistic for those which fall in between.

There are additional caveats to account for when the sensors reach the quantum regime—some nanothermometers can, in fact, be as small as individual atoms or electrons.[21–23] To work as temperature sensors these quantum systems should ideally show "thermal" characteristics, i.e., the temperature should be a monotonic function mappable onto the expectation value of an observable. Briefly, this is easier to understand for a quantum-sensor, which is only weakly correlated to the heat bath of the larger surrounding system and can be described through mean-field, perturbation theory. In this case the temperature becomes a monotonic function that can be mapped continuously, for instance, on the energy of the sensor's quantum state. Less obvious is the scenario of a quantum-sensor, which is strongly correlated to the local environment. In this case, the overall sensor–object system is described through a many-body-model in which the wavefunctions are strongly interdependent. The sensor could be much more susceptible to local fluctuations other than temperature (e.g., spin-flip events), which would hinder its use as a temperature sensor or limit its signal resolution due to a lower signal-to-noise ratio (cf. Section 2.2.2). Real (quantum) systems usually lie in between these extreme descriptions and their specificities (e.g., coherence time[21,22]) should be considered when determining both spatial and signal resolution for temperature measurement.

2.2.2. Signal Resolution and Sensitivity

Signal resolution and sensitivity are often used interchangeably. While being both crucial in determining the ability of a technique to resolve the changes of an observable, they are fundamentally different.

Sensitivity is an absolute quantity: it specifies the smallest, absolute amount of change that can be detected by the sensor. The emphasis is on the absolute relationship between the independent (i.e., temperature, T) and the dependent variable (i.e., measured observable, O): intuitively, a "steeper" derivative ($\partial O/\partial T$) corresponds to a higher sensitivity.

~~Resolution,~~ ~~unlike~~ sensitivity, resolution is a relative quantity. It is the degree to which a change can be detected. The emphasis is on the smallest change detectable over the noise and it is thus often referred to as noise-floor measurement. It is a relative quantity: it can be improved for instance by sacrificing temporal bandwidth, i.e., by integrating the signal for a longer time to average-out the noise. For this reason, it is generally expressed, for temperature measurements, in K Hz$^{-1/2}$. In determining the resolution of a nanothermometry technique it is also important to consider the fundamental limit set by thermodynamics on the concept of temperature (cf. Section 2.2.1). Due to the small size, the temperature of a nanoparticle experiences fluctuations that can be quantified via the standard deviation σ_{th} expressed as[24] Q6

$$\sigma_{\mathrm{th}} = T\sqrt{\frac{k_{\mathrm{B}}}{VC_V}} \tag{1}$$

where k_{B} is the Boltzmann constant, V is the volume of the nanoparticle, and C_V is its constant volume heat capacity per unit volume. The characteristic time scale of these fluctuations, τ_{rel}, is defined by the heat exchange between the particle and its environment. A nanoparticle in a homogeneous medium has τ_{rel} on the order of a^2/α, where a is the radius of the crystal and α is the thermal diffusivity of the medium. The thermal fluctuations can be determined as $\sigma_{\mathrm{th}}\sqrt{\tau_{\mathrm{rel}}/t_{\mathrm{m}}}$, where t_{m} is the integration time of the measurement. The limit on the noise floor $\eta_{\mathrm{th},T}$ is thus set by the thermal fluctuations and can be estimated as

$$\eta_{\mathrm{th},T} = \sigma_{\mathrm{th}}\sqrt{\tau_{\mathrm{rel}}} \approx T\frac{k_{\mathrm{B}}}{\sqrt{aC_V\alpha}} \tag{2}$$

The resolution of a technique should always be evaluated against this noise floor limit $\eta_{\mathrm{th},T}$.

In this review, we discuss the sensitivity and resolution of selected nanothermometry techniques separately. Note also that, in general, we benchmark different techniques using the so-called relative sensitivity, defined as[7,23]

$$S_{\mathrm{r}} = \frac{\partial O/\partial T}{O} \tag{3}$$

which allows for standardizing the various methods regardless of the difference in underlying working principle—and measured observable, O.

2.2.3. Range

Every thermometry technique is based on a set of physicochemical relationships that hold—or work optimally—in a specific range of temperatures. Range might prevent the practical use of a method in specific applications (e.g., a nanoparticle-based sensor that is not chemically stable at high temperatures is not suitable for high-power electronics measurements). Notably, certain nanothermometers (e.g., those based on color centers in nanodiamonds (NDs); cf. Section 3.4) can have multiple working mechanisms, which allows for switching between them based on the temperature range they are optimal at. It should be noted that often sensitivity and resolution can be temperature-dependent, i.e., better or worse depending on which temperature range the sensor operates at.

2.2.4. Accuracy, Precision, Reproducibility, and Stability

Thermometers can be benchmarked based on a series of other characteristics, which are ubiquitous and applicable to any type of sensor. A nanothermometer should be accurate and precise—the reading should be close to the true value of temperature, with no dispersion among its measured values. It should be reproducible and stable—it should maintain accuracy over consecutive thermal cycles and its measurement should stay consistent over time. Fast response, which is associated with small heat capacity and good thermal contact, is also desirable characteristic. In general, in this review these factors are considered in cases where a technique either shows limitation or excellence in performance with respect to other techniques.

2.2.5. Utility

While there is not a rigorous definition of utility, in this review, we highlight techniques which, owing to their unique convenience or ease-of-measurement, have a wider range of applicability than homologous alternative methods. For instance, an all-optical thermosensing technique based on mapping temperature, noninvasively, onto the fluorescence intensity of the nanothermometer ranks higher in utility than one that requires measuring, with direct access to the object, a combination of multiple signals or quantities.

2.2.6. Limitations and Thermal Equivalent Noise (TEN)

One aspect often overlooked when discussing nanothermometry techniques is the assessment of their reliability, especially in nonideal practical applications where it might be hard to control for every parameter affecting the temperature reading. In certain cases, effects other than temperature can alter the value of the observable onto which temperature is mapped. This means that the measured value might not be an accurate reading of the true temperature, but rather TEN.[25] Effects known to give rise to TEN are, for instance: i) variable response of the nanothermometers to different laser excitation powers, ii) self-absorption by the nanoprobe of its own photoluminescence, iii) wavelength-dependent absorption and scattering of light by the environment, iv) apparent wavelength shifts caused by absorption/emission of the surroundings, which can alter the spectral shape of the signal, and v) heating of the nanosensor either due to laser absorption or nonradiative, phonon-assisted decay processes.

These effects can be partially mitigated by, for instance: monitoring the response of the sensor i′) under different excitation powers, ii′) at different depths in the sample, and iii′) off- and in situ—all while temperature is kept constant, to quantify the (sample-specific) TEN.

In this review, we discuss the main sources of thermal equivalent noise specific to each type of nanothermometer.

3. Thermometers Based on Nanoparticles

This class of nanothermometers consists of nanoparticles placed in direct contact with the object to be sensed. Most nanoparticle-based thermometers provide temperature readings through temperature-associated changes in an observable—e.g., photoluminescence intensity, emission wavelength, full width at half maximum (FWHM), lifetime, etc. They are semi-invasive as they tend to have a negligible impact on the target system. This is due to their relatively small size and ability to be dispersed over the object, which allows for the probing of local temperatures in different target regions during the same measurement.

In contrast, thermometers such as thermocouples and fiber-optic sensors are considered invasive, as they require relatively bulkier inserts to probe the object, often in multiple locations.[26]

Finally, techniques such as computerized tomography (CT), photoacoustic, infrared thermography, and magnetic resonance imaging (MRI) thermometry are deemed noninvasive as the measurement does not require a physical sensor to be in contact with the system.[26]

In this review we discuss a selection of nanoparticle-based thermometers for which the readout of the temperature is done optically, i.e., through monitoring of their photoluminescence and associated observables. These techniques are summarized in **Table 1** and are described in detail in Sections 3.1–3.4. **Figure 1** displays the relative sensitivity S_r and operating temperature of some of these techniques, for direct comparison.

3.1. Organic Dyes

Organic dyes are fluorophores, which display temperature-dependent photoluminescence intensity and lifetime and can thus be used for thermosensing applications. One of their main advantages over other nanothermometer candidates is their versatility. There is a vast range of available—and even designable—organic fluorophores tailored for parameters including absorption and emission wavelength, spectral range, solubility, and ability to be functionalized to target specific analytes.

3.1.1. Fundamental Mechanism(s)

Organic dyes are compounds of carbon-based molecules, which display strong photoluminescence under optical excitation. Their spectral properties depend on their specific molecular species, symmetry, and structure, as well as factors such as surrounding solvent or host-matrix, concentration, pH, and temperature. The fundamental mechanisms behind the photoluminescence versus temperature dependence do differ for different classes of molecular dyes, but it is possible to identify a few general principles.

Fluorescence Quenching: A first class of dye-nanothermometers consists of molecules whose photophysics is susceptible to a series of factors—including temperature—which can alter the dye's quantum yield and thus its photoluminescence signal. The temperature-dependent quenching mechanism might vary from dye to dye, but the generalized, fundamental photodynamics can be described resorting to the Jablonski energy-level model (**Figure 2**a).

From the ground state—usually a singlet state, S_0—the molecule can absorb a photon and be excited into singlet or triplet states, S_i and T_i ($i \geq 1$), respectively. Note that each electronic state has different vibrational and rotational states and the energy of the first excited triplet state T_1 is normally lower than the energy of the corresponding singlet state S_1.

Table 1. Benchmarking of various nanothermometers: sensitivity and temperature range.

	Nanothermometer[a)][ref]	S_r [K^{-1}] at 300 K	$S_{r,m}$ [K^{-1}] at (T_m)	ΔT [K]
ODs	Ruphen (PL intensity)[27]	0.0093	0.0114 (273)	280–315
	Bis(pyrene) propane (PL ratio)[28]	0.387	0.256 (310)	310–465
	Rhodamine-B (PL Intensity)[29]	0.02	0.0267 (287)	287–363
	Fluorescein (PL anisotropy)[30]	0.057	0.069 (293)	293–352
	Triarylboron (wavelength shift)[31]	0.005	0.0078 (373)	223–373
QDs	CdSe (wavelength shift)[32]	1.61×10^{-4}	1.61×10^{-4} (293)	293–323
	CdSe/ZnS (PL intensity)[33]	0.019	0.025 (313)	278–313
	CdSe/ZnS (wavelength shift)[34]	2.67×10^{-4}	2.68×10^{-4} (287)	284–320
	Zn$_{1}$_xMnxSe/ZnCdSe (PL ratio)[35]	0.018	0.07 (134)	134–400
	CdTe (PL lifetime)[36]	0.008	0.011 (333)	293–333
UCNPs	Er^{3+}/Yb^{3+} CaF_2 (PL ratio)[37]	0.015	0.02 (318)	293–318
	Tm^{3+}/Yb^{3+} CaF_2 (PL ratio)[37]	0.002	0.002 (318)	293–318
	$NaYF_4$:Er^{3+}, Yb^{3+} (PL ratio)[38]	0.0114	0.0116 (298)	298–334
	$NaLuF_4$:Yb, Er (PL ratio)[39]	0.009	0.011 (273)	273–348
	ZnO:Er^{3+} (PL ratio)[40]	0.0098	0.011 (278)	278–463
	β-$NaYF_4$:20%Yb2%Er (PL ratio)[41]	0.0157	0.0164 (294)	294–334
	$(Gd,Yb,Er)_2O_3$ (PL ratio)[42]	0.017	0.017 (300)	300–1050
NDs	NV (PL intensity)[43]	0.01	0.01 (295)	295–400
	GeV (ZPL linewidth)[44]	0.0064	0.0064 (305)	150–400
	SiV (ZPL shift)[45]	1.61×10^{-5}	1.61×10^{-5} (285)	285–305
	SnV (ZPL shift)[46]	8.66×10^{-5}	8.67×10^{-5} (295)	295–315
	GeV (anti-Stokes)[23]	0.014	0.13 (150)	150–400

[a)] Benchmarking of a selection of nanothermometry techniques, organized by type: organic dyes (ODs; green), quantum dots (QDs; violet), upconversion nanoparticles (UCNPs; orange), and nanodiamonds (NDs; cyan). The table lists, for each technique, the basic mechanism, the relative sensitivities S_r at 300 K, and $S_{r,m}$ at the temperature T_m where the relative sensitivity is the highest, and the temperature working range ΔT.

Q7

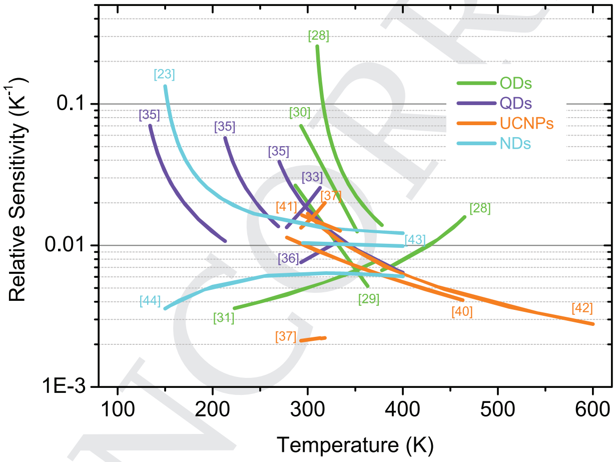

Figure 1. Relative sensitivity $S_r = (\partial O/\partial T)/O$ versus temperature for a selection of nanothermometry techniques. These have been extracted from published data (corresponding references are indicated on the graph). The curves are color-coded as per Table 1: organic dyes (green), quantum dots (violet), upconversion nanoparticles (orange), and nanodiamonds (cyan).

Furthermore, the singlet–singlet transition, $S_0 \leftrightarrow S_i$, is more probable than the singlet–triplet transitions $S_0 \leftrightarrow T_i$, as the latter involves a change in spin multiplicity. After absorption of a photon, the dye molecule from the excited singlet state S_i ($i > 1$) quickly relaxes (timescale approximately ps) to the lowest singlet state S_1 through internal conversion (IC) and without emission of a photon. It then decays back to the ground state S_0 either radiatively (fluorescence) or nonradiatively (through IC or external conversion (EC)). Alternatively, it can undergo the radiationless, spin-forbidden $S_1 \rightarrow T_1$ transition between two states of different multiplicity (intersystem crossing (ISC)). The subsequent transition $T_1 \rightarrow S_0$ is either radiative (phosphorescence) or nonradiative (ISC or EC). The decay $S_1 \rightarrow S_0$ is faster than $T_1 \rightarrow S_0$ as the latter is a spin-forbidden radiative transition between two states of different spin multiplicity. Note that the EC process refers to interactions between the excited molecule and the surrounding environment (e.g., with the solute). These processes are photoluminescence-quenching processes and can involve different mechanisms including energy transfer or collision/diffusion-induced interactions between the dye and the nearby atoms and molecules. The population of the excited singlet state (S_1) and triplet state (T_1) depends on the competition among all these different photophysical processes and can be generalized by the system of coupled equations

$$\frac{d[S_1]}{t} = k_{S_1}\,[S_0] - (k_{r,f} + k_{ic} + k_{isc,S_1-T_1} + k_{ec,S})[S_1] + k_{isc,T_1-S_1}[T_1] \tag{4}$$

$$\frac{d[T_1]}{t} = k_{isc,S_1-T_1}\,[S_1] - (k_{r,p} + k_{isc,T_1-S_0} + k_{isc,T_1-S_1} + k_{ec,T})[T_1] \tag{5}$$

where $I_a = k_{S_1}\,[S_0]$ is the light absorption rate proportional to the population $[S_0]$ in the ground state and the rate constant of excitation k_{S_1}. The quantities $k_{r,f}$ and $k_{r,p}$ are the radiative rate constants for fluorescence and phosphorescence; k_{isc,S_1-T_1}, k_{isc,T_1-S_0}, and k_{isc,T_1-S_1} are the rate constants for the intersystem crossings $S_1 \rightarrow T_1$, $T_1 \rightarrow S_0$, and $T_1 \rightarrow S_1$, respectively. The quantity k_{ic} is the rate constant for the internal conversion, while $k_{ec,S}$ and $k_{ec,T}$ are the rate constants for the external conversion quenching in the singlet and triplet states.

The reason molecular dyes of this type can be used as nanothermometers lies in the fact that some of the rates in Equations (4) and (5) are temperature dependent. As the temperature changes, so does the relative probability for the excited molecule to decay to the ground state via the radiative or nonradiative path(s)—effectively altering the molecule's photoluminescence intensity (and lifetime). It should be remarked that the change in decay rates with temperature can involve

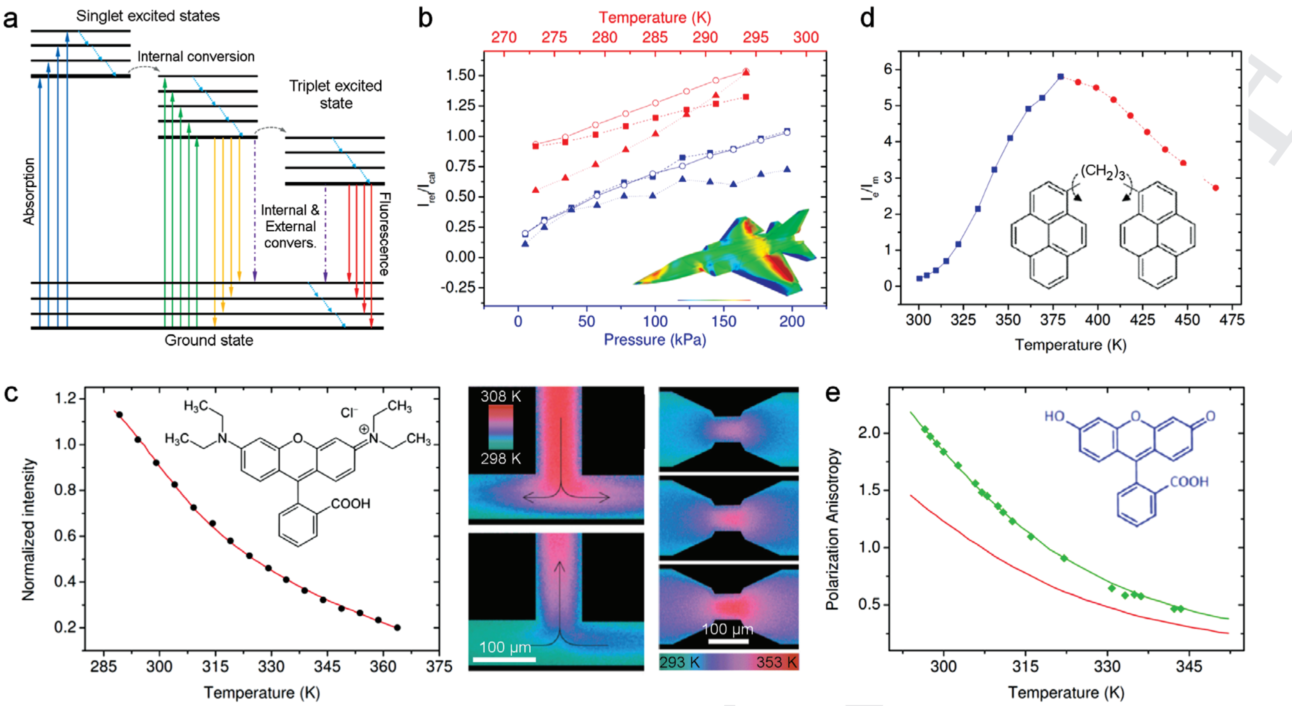

Figure 2. Fundamentals of organic dyes nanothermometry. a) Jablonski energy-level model illustrating the main excitation and decay processes in organic molecules. b) Fluorescence-based temperature (red) and pressure (blue) measurement using three pressure-sensitive paints containing molecular dyes: ODU (empty circles), MCD (squares), and UWA (triangles). Temperature measurements are taken at a constant pressure of 197 kPa and pressure measurement at a constant temperature of 273 K. Adapted with permission.[27] Copyright 1998, Springer-Verlag. Inset: representative pressure distribution measured on the surface of a model plane (size ≈1.2 × 1.0 m^2) in a wind tunnel. Adapted with permission.[62] Copyright 2005, Springer-Verlag. c) Dependence between the normalized intensity of Rhodamine B (inset) in deionized water and temperature (graph, left), used to measure the temperature distribution in various microfluidic structures due to Joule heating (heat maps, right). Adapted with permission.[29] Copyright 2001, American Chemical Society. d) Temperature mapping based on the excimer–monomer relative fluorescence in bis(-pyrene) propane (inset). Note the monotonic increasing (blue squares, 300–375 K) and decreasing (red circles, 375–465 K) dependence for different temperature ranges. Adapted with permission.[28] Copyright 1998, John Wiley & Sons. e) Temperature measurement based on polarization anisotropy of fluorescein (inset) dissolved in a glycerol–water mixture. Theoretical curve (solid green line) and experimental measurements (green diamonds) along with the calculated corrected curve (red solid line) due to the use of a high-NA objective in the experiments. Adapted with permission.[30] Copyright 2009, Optical Society of America.

complex and competing effects. Therefore, dye-nanothermometers of this type require calibration against a set of reference temperatures.

Nanothermometers of this type have been extensively used, for instance, in aerodynamics (Figure 2b) where dyes are mixed with paints to monitor pressure and temperature on aerodynamic and aircraft surfaces.[47,48,27] These so-called pressure-sensitive paints (PSP) work on the principle that oxygen can quench—via the aforementioned external conversion mechanism—the photoluminescence of certain dyes such as Rhodamine B, platinum porphyrins, ruthenium polypyridyls, pyrene derivatives,[49] β-diketone chelates of Tb^{3+}, Eu^{3+} and Sm^{3+},[50] to cite a few. Briefly, optical illumination drives the dye molecules to the excited state from which they decay to the ground state either radiatively, emitting photons at longer wavelengths, or nonradiatively. Oxygen can quench the dye's photoluminescence by providing an additional nonradiative decay path, which competes with the radiative one. The total decay rate of the dye molecule can be written following the Stern–Volmer model

$$\tau^{-1} = k = (k_r + k_{nr}) + pk_q \tag{6}$$

where for simplicity k_r and k_{nr} collect all the (intrinsic) radiative and nonradiative decay rates listed explicitly in Equations (4) and (5), k_q is the (extrinsic) nonradiative decay rate due to the interaction with oxygen (equivalent to $k_{ec,S}$ and $k_{ec,T}$ in Equations (4) and (5)), and p is the oxygen pressure. In general, the rate constants k_{nr} and k_q for the nonradiative and quenching processes are temperature dependent. The inverse of the rate k is the molecule's lifetime τ. Note that Equation (6) is general and can refer to any experimentally observed photoluminescence process, i.e., it can either refer to the molecule's fluorescence ($S_1 \rightarrow S$) or phosphorescence ($T_1 \rightarrow S_0$). Also, while the rightmost term in Equation (6) refers explicitly to the case of oxygen-driven (collisional) quenching, the equation can be adapted to include terms for different quenching effects (e.g., for Forster resonant energy transfer, FRET),

$$\tau^{-1} = k = (k_r + k_{nr}) + \sum_j C_j k_j \tag{7}$$

where each rate k_j (with corresponding relevant parameter(s) C_j) refers to a specific external conversion decay channel.

The quantum yield η of the dye molecule is defined as the ratio between the radiative and the total (radiative plus nonradiative) decay rates

$$\eta = \frac{k_r}{k_r + k_{nr} + pk_q} \tag{8}$$

From Equations (6) and (8), the ratio between the quantum yield η_0 at a reference pressure p_0 and the quantum yield η at ~~at~~ any other pressure p is given by the expression

$$\frac{\eta_0}{\eta} = \frac{k_\mathrm{r} + k_\mathrm{nr} + pk_\mathrm{q}}{k_\mathrm{r} + k_\mathrm{nr} + p_0 k_\mathrm{q}} = \frac{I_0}{I} \tag{9}$$

where the far-right equality holds as the photoluminescence intensity I is proportional to the quantum yield. Equation (9) can be written in the more compact form

$$\frac{I_0}{I} = A + B\left(\frac{p}{p_0}\right) \tag{10}$$

where $A = (k_\mathrm{r} + k_\mathrm{nr})/(k_\mathrm{r} + k_\mathrm{nr} + p_0 k_\mathrm{q})$ and $B = (p_0 k_\mathrm{q})/(k_\mathrm{r} + k_\mathrm{nr} + p_0 k_\mathrm{q})$ are determined experimentally and such that $A + B = 1$, while I_0 is the photoluminescence intensity measured at a reference pressure p_0. Note that Equation (10) establishes a direct relation between pressure and photoluminescence intensity (and lifetime) of the dye molecules. Temperature comes into play indirectly as the coefficients A and B depend on temperature via k_nr and k_q. Temperature acts in two ways. On the one hand, the nonradiative decay rate k_nr can be decomposed into two components, one independent ($k_{\mathrm{nr},0}$) and one dependent ($k_{\mathrm{nr},T}$) on temperature (T)—with the latter displaying an Arrhenius-type behavior, i.e.

$$k_\mathrm{nr} = k_{\mathrm{nr},0} + k_{\mathrm{nr},T}\mathrm{e}^{\left(-\frac{E_\mathrm{nr}}{k_\mathrm{B}T}\right)} \tag{11}$$

where E_nr is the activation energy for the nonradiative process(es) and k_B is the Boltzmann constant. On the other hand, temperature can also affect oxygen diffusion in the polymer matrix—the paint—hosting the dye. For a diffusion-limited quenching reaction, the quenching rate k_q is given by the Smoluchowski equation

$$k_\mathrm{q} = 4\pi N\sigma(R_\mathrm{p} + R_\mathrm{q})(D_\mathrm{p} + D_\mathrm{q}) \tag{12}$$

where D_p and D_q are the diffusion coefficients of the probe (i.e., the dye molecules) and the quencher (i.e., oxygen) in the polymer, while R_p and R_q their respective molecular radii; N is the number of molecules per millimole and σ is a factor that depends on the quenching mechanism and is related to the probability of each collision to cause quenching[51] The diffusion coefficients D_i $(i = \mathrm{p}, \mathrm{q})$ also depend on temperature and are described by the Stokes–Einstein equation

$$D_i = \frac{k_\mathrm{B}T}{6\pi\mu R_i} \tag{13}$$

where μ is the viscosity of the host or solvent. Under constant pressure, the dye molecules can thus be used as nanothermometers since the parameters A, B, and D_i all depend on temperature and affect the molecules' photoluminescence intensity.

As discussed above, due to the complex temperature-dependent dynamics of these rates, calibration of the dyes' photoluminescence signal against a known set of temperatures is required for use in nanothermometry. Also, while this analysis is applicable to both fluorescence (singlet-to-singlet decay) and phosphorescence (triplet-to-singlet decay), the latter is usually much more susceptible to extrinsic (oxygen-driven in this case) quenching, in virtue of its longer radiative lifetime involving the triplet state of the molecule. The inset in Figure 2b shows how pressure sensitive paints can be used to measure pressure loads over the surface of an aircraft in a wind tunnel using the Stern–Volmer model of Equation (10). A similar map can be realized for temperature, either by operating at constant pressure or by using a polymer binder impermeable to oxygen to avoid the external conversion quenching (i.e., $k_\mathrm{q} \approx 0$). The aircraft is obviously a macroscopic object, but the pressure and temperature on its surfaces can be read with a spatial resolution that is ultimately determined by the resolution of the optical system used to detect it (approximately diffraction limit). The sensitivity of this class of dye-nanothermometers is the order of ≈0.5–4% K^{-1} in the range ≈90–800 K, but limited to approximately tens of K per each type of dye.[49] Figure 2b shows the pressure and temperature mapping onto the photoluminescence intensity of three dyes based on ruthenium (ODU, MCD) and platinum octaethylporphyrin (UWA) compounds.[52] Note that to avoid the practical complications due to the dual pressure-temperature dependence, the organic molecules can be encapsulated in polymer shells with low oxygen permeability. In this case the quantum yield is simply

$$\eta = \frac{k_\mathrm{r}}{k_\mathrm{r} + k_\mathrm{nr}} \tag{14}$$

Using the temperature dependence for k_nr from Equation (11) in Equation (14), we can write

$$\ln\frac{I_T\left[I_0 - I_{T_\mathrm{ref}}\right]}{I_{T_\mathrm{ref}}\left[I_0 - I_T\right]} = \frac{E_\mathrm{nr}}{k_\mathrm{B}}\left(\frac{1}{T} - \frac{1}{T_\mathrm{ref}}\right) \tag{15}$$

where $I_0 = I(T = 0)$ and $I_\mathrm{ref} = I(T = T_\mathrm{ref})$ are the photoluminescence intensity at absolute zero and at a reference temperature T_ref, respectively, while $I_T = I(T)$ is the photoluminescence intensity at the temperature T to be determined. For $\left|I_T - I_{T_\mathrm{ref}}\right|/I_0 \ll 1$ and $I_T I_{T_\mathrm{ref}}/I_0^2 \ll 1$ over a certain temperature range, Equation (15) can be approximated by the Arrhenius form

$$\ln\frac{I_T}{I_{T_\mathrm{ref}}} = \frac{E_\mathrm{nr}}{k_\mathrm{B}}\left(\frac{1}{T} - \frac{1}{T_\mathrm{ref}}\right) \tag{16}$$

Note that the Arrhenius plot of $\ln(I_T/I_{T_\mathrm{ref}})$ versus $1/T$ gives a linear slope of $E_\mathrm{nr}/k_\mathrm{B}$ usually over only a limited range of temperatures, which again highlights the fact that a calibration curve should be used in practical applications.

Examples of dye-based, temperature sensitive compounds that are independent of pressure include, for instance, PtTFPP and Ruphen molecules embedded in polyacrylonitrile (PAN) nanoshells.[27] Their photoluminescence shows temperature dependence with sensitivities of the order of 1.1% K^{-1} for the PtTFPP-PAN and 1.4% K^{-1} for the Ruphen-PAN complexes (in the range ≈280–320 K), and are nearly independent of pressure, making them more robust temperature nanosensors. In the Ruphen-PAN case, the particularly robust insensitivity to pressure is due to both the PAN shell preventing oxygen from quenching the fluorescence, and the intrinsically short lifetime of the dye (<1 µs).

Besides application in aerodynamics, molecular dyes of this class have been successfully used to map temperatures and temperature gradients inside microfluidic systems.[29,53,54] One of the first and most representative examples of this technique used Rhodamine B molecules diluted in deionized water flowing in microfluidic channels (Figure 2c).[29] After calibration of the photoluminescence intensity-versus-temperature response, the solution was electrokinetically pumped through complex, multibranched microfluidic circuits with steep angles and constrictions to map the temperature distribution of the solution at these critical points as a consequence of Joule heating. Figure 2c shows the temperature mapping achieved with such technique; the sub-micrometer spatial resolution is given by the optical microscope used for detection (approximately diffraction limit) while the sensitivity achieved was ≈1–2% K^{-1} over the range 290–360 K. Similar approaches based on coating the structure to map with thin films of thermosensing dyes have also been developed.[55,56] These coating-based methods though have two main drawbacks. They are only capable of measuring 2D, surface temperature distributions and can potentially have a non-negligible thermal load capable of altering the temperature of the surface itself.

These photoluminescence dyes have also been used in biological settings, where the temperature of specific organelles within cells has been mapped onto variations of the luminescence intensity and lifetime of the molecular dyes (cf. Section 4.1).[57–61]

Photoluminescence Lifetime: Analysis of Equation (7) reveals that PL quenching is directly related to changes in lifetime. This is due to temperature—as well as effects such as resonant energy transfer, intersystem crossing or external conversion processes—affecting the relative contribution of radiative and nonradiative rates, which then result in changes of the dye's measured lifetime. Mapping temperature changes onto variations in photoluminescence lifetime can be advantageous. In PL intensity measurements higher resolutions are achieved through increasing the signal-to-noise ratio by integrating for longer times. This can be problematic in thermometry measurements as long laser excitation can result in local heating and thus incorrect temperature reading. Conversely, lifetime measurements can be carried out with fast photodetectors with a high signal-to-noise ratio (e.g., avalanche photodiodes or photomultipliers) rather than spectrometers, and with relatively shorter integration times (individual excitation–emission cycles for dyes are usually in the ns–ms time scale). Temperature-driven changes in the lifetime of, for instance, Rhodamine B[63–65] and Kiton Red[66] (a water-soluble, sulfonated derivative of Rhodamine B) dyes have been effectively used for thermosensing applications.

Monomers–Excimer Fluorescence: Another class of dye-based nanothermometers is that of excimer-forming dyes. One example of such dyes is bis(-pyrene) propane (BPP),[28] which can be used as a model to understand the mechanism behind the temperature-dependent photoluminescence of this class of dyes. Bis(-pyrene) propane consists of fluorescent monomers (pyrene rings) connected through a flexible propyl alkane linkage. As one monomer is excited by UV light (at ≈345 nm) it can decay radiatively (fluorescence at ≈380 and ≈400 nm) or nonradiatively with rates k_r and k_{nr}, respectively. Alternatively, the excited monomer can form, with rate k_{ov}, an excimer with the nearby unexcited monomer by overlapping with it, upon rotating around the flexible bond. This can often involve interaction between the π-electrons of the excited and unexcited monomers to establish a stable molecular excimer. In analogy with the monomer, the newly formed excimer can decay radiatively or nonradiatively with respective rates k_r' and k_{nr}', or dissociate back, with rate k_d, to the excited-plus-ground monomer pair. When decaying radiatively, the excimer fluoresces at longer wavelengths than the monomer and its spectrum is broad and featureless. The ratio of the excimer to monomer fluorescence intensity I_e/I_m is given by[67]

$$\frac{I_e}{I_m} = \frac{k_r' k_{ov}}{k_r (k_d + k')} \tag{17}$$

where k' is the total decay rate of the excimer. The resulting fluorescence spectrum is temperature dependent as both the rates k_{ov} and k_d vary with temperature. This dependence however is not straightforward. The rate k_{ov} for an excited pyrene ring to rotate to the excimer position depends on the intramolecular rotational relaxation rate: $k_d \sim CT\mu$, where C is a constant, T is the temperature, and μ is the molecular viscosity in the proximity of the excimer. The viscosity varies with both temperature and pressure following an Arrhenius-type relation. Dye-nanothermometers of this type have been used, for instance, mixed in polymer and resin matrices to measure the substance temperature during extrusion.[28,68] In these cases the overlap rate k_{ov}, has been shown to vary with temperature following empirical equations.[69] As the temperature increases so does the fraction of free volume in the polymer host alongside the molecules' motility and thus the rate k_{ov}. Correspondingly, the fluorescence ratio I_e/I_m increases with temperature, Equation (17), so long as the dissociation rate is slower than the excimer decay rate, i.e., $k_d \ll k'$ (Figure 2d, blue squares). However, once the excimer state is formed, its dissociation rate obeys itself to an Arrhenius-type law with its activation energy being associated to breaking the intramolecular bond. Simultaneously, as the temperature increases, the dissociation rate k_d increases until it can drive the ratio I_e/I_m to switch, Equation (17), from being an increasing function of temperature to being a decreasing one (Figure 2d, red circles).

Analysis of this complex temperature dependence calls for a couple of important observations. The practical use of this class of excimer-forming dyes as thermosensors requires calibration against a set of reference temperatures. Furthermore, the trends ruled by k_{ov} and k_d can be competing,[28] and the observable I_e/I_m might go from being a monotonically increasing function of temperature to be a monotonically decreasing one—which requires prior knowledge of the operating range to unequivocally correlate values of fluorescence and temperature. Note that similarly to the case of pressure-sensitive paints, due to the dependence between the fraction of free volume (and associated molecular viscosity μ) and k_{ov}, this class of dyes has also been employed to measure hydrostatic pressure effects on polymers via changes in photoluminescence intensity and lifetime.[69,70] Analogous methods based on monomer–excimer conversion have been shown to achieve temperature measurement sensitivities as high as ≈4.5% K^{-1}, over the range 290–335 K.[71]

Monomers–Exciplex Fluorescence: Very similar to the class of excimer-based nanothermometers is that of exciplex-forming dyes—an exciplex is the equivalent of an excimer but with the molecules involved being of different species. The underlying mechanism can be generalized using a two-state equilibrium model. The molecules of different species can exist in equilibrium either as separate monomers or as an exciplex. Temperature affects the number of molecule-pairs existing in one equilibrium state relative to the other.

A representative example is that of perylene and *N*-allyl-*N*-methylaniline (NA) molecules in a soft elastic polystyrene matrix.[72] The photoemission from the compound shows spectral features at 463 and 475 nm (attributed to perylene monomers) as well as a broad band centered at 551 nm (attributed to exciplex formation between perylene and NA); NA alone is nonemissive in the considered spectral excitation/emission regions. As the temperature increases, the ratio between the emission at the lower wavelengths (463 and 475 nm) and at longer wavelengths (551 nm) increases with an isoemissive, unchanging point at 543 nm.

The ratio $I_\mathrm{m}/I_\mathrm{e}$ between the relative intensity follows an Arrhenius-type relation where the activation energy E_a is the activation enthalpy between the two equilibrium states. Note that, conveniently, this measurement is ratiometric, i.e., self-referencing, with a spatial resolution determined by the resolution of the optical microscope (i.e., diffraction limited). In this specific example, the reported sensitivity of the technique was ≈1% K^{-1}, over the range 298–358 K. An aspect to consider for the utility of the technique is the importance of controlling the relative concentration of the molecules of different species to maximize the change in PL intensity ratio as the temperature changes.

Twisted Intramolecular Charge Transfer (TICT) Fluorescence: TICT compounds are molecules, which can exist in two different photoluminescent excited states.[73] They belong to a wide family of molecules, typically heteroaromatic compounds, which can undergo intra- and intermolecular photochemical reactions in the excited state leading to different molecular conformations as well as relaxation processes. Representative examples include pyrene-containing triarylboron molecule compounds[31,74] and (*N*,*N*-dimethylamino)benzonitrile (DMABN) compounds,[75] which can show two intrinsic fluorescence bands, one originating from the so-called local excited state (LE, short wavelengths) and the other from the TICT state (long wavelengths). The probability of each molecule to be in one of the two states depends on several factors including the polarity and viscosity of the surrounding microenvironment as well as temperature. Careful choice of both the compounds and the surrounding microenvironment (e.g., via microencapsulation of the dye)[74] can lead the fluorescence response to be almost solely driven by temperature. The fluorescence response is characterized both by a change in the dye's quantum yield—which increases as temperature increases—and in emission wavelength—e.g., from orange–red (≈590 nm) to green–yellow (≈560 nm). Temperature sensing using this method has been shown to achieve sensitivities of ≈0.1% K^{-1}, over the range 243–413 K, with a spatial resolution of 4 µm.

Spin Crossover: Another class of molecule-based nanothermometers is that of spin crossover molecular materials. These typically consist of molecular metal complexes showing bistability, i.e., the ability to exist in two stable states for a given range of perturbations.[76] This occurs, for instance, in some transition metal ions for which the d-orbitals lose degeneracy when interacting with ligands. According to crystal field theory, these transition-metal complexes can exhibit a low-spin (LS) ground state and a high-spin (HS) ground state (metastable) electron configuration of the metal's d atomic orbitals. The quantum LS state in its equilibrium geometry is slightly more stable (i.e., lower energy) than the HS state, also in its equilibrium geometry, but the complex can cross over—bidirectionally—between the two states, LS ↔ HS. At low temperature, LS is the thermodynamically stable state, but above a certain threshold temperature $T_{1/2}$, the thermodynamically stable state is the HS one. This is due to the competition between enthalpy, which favors the low-energy fundamental state (LS) at low temperatures, and entropy, which favors the most disordered thermodynamic phase (HS) at high temperatures and compensates for the energy increase. The temperature $T_{1/2}$ is the temperature at which there is equal probability for the system to be in the LS and HS state. For completeness, the LS → HS crossover can be induced by other stimuli other than temperature, including pressure, and light irradiation.[77]

When the other parameters are controlled for, a change in temperature can induce the spin crossover, which is accompanied by a change in the absorption and emission optical properties of the molecules. In more advanced applications, these bistable molecular metal complexes have been chemically linked to photoluminescent subunits whose fluorescence is quenched as a function of temperature through interaction with the metal ions of the complex. Nanothermometers of this kind have been demonstrated, for instance with Fe-based[78,79] (sensitivity ≈2% K^{-1}, over the range 305–325 K) and Ni-based complexes linked to fluorescent molecular segments[80] (sensitivity ≈3–4% K^{-1}, over the range 300–338 K). For these nanothermometers, calibration curves are required. Their photodynamics is complex—dictated by the energies of the LS and HS states, as well as by the photoluminescence-quenching effects, which are due to the interaction of the fluorophore molecule with the metal ions (e.g., via electron transfer and energy transfer) and which depend on which state (LS or HS) the bistable molecule is in.[80]

Polarization Anisotropy Fluorescence: When an ensemble of photoluminescent molecules is excited optically by a linearly polarized laser beam, the re-emitted photoluminescence is only partially polarized due to the random orientation of the molecule transition dipole moments with respect to the electric field vector of the excitation light. The so-called polarization anisotropy (ϱ) is thus the ratio between the two possible output polarizations–parallel ($I_\parallel$) and perpendicular ($I_\perp$) to the excitation polarization[81]

$$\varrho = \frac{I_\parallel - I_\perp}{I_\parallel + 2I_\perp} \tag{18}$$

Assuming that the angle between the molecule's absorption and emission dipoles is zero, geometric considerations give a theoretical value of ϱ = 0.4. Note that experimental values are usually lower due to depolarization factors including secondary fluorescence, excitation energy migration between molecules, rotational motions and torsional vibration of the molecules. Also note that the angle between the absorption and emission dipoles can be nonzero if, for instance, the molecule is excited to higher energy levels from which it then decays via radiationless conversion to the level of its main fluorescence. Temperature affects the measured value for ϱ due to molecular rotation related to Brownian motion, specifically

$$\frac{1}{\varrho} = \frac{1}{\varrho_0}\left(1 + \frac{\tau_F}{\tau_R}\right) \tag{19}$$

where ϱ_0 is the value for ϱ at a reference temperature, while τ_F and τ_R are the molecules' fluorescence lifetime and the rotational relaxation time, respectively. The quantity τ_R depends on temperature (T) through the Debye–Stokes–Einstein equation

$$\tau_R = \frac{V\mu}{k_B T} \tag{20}$$

where V is the hydrodynamic volume of the molecule, μ is the viscosity of the solvent, and k_B is Boltzmann constant. Equation (19) highlights how the measured fluorescence anisotropy ϱ depends on the relative rate at which, on average, the molecules rotate with respect to their fluorescence decay rate. Since τ_R depends on temperature, Equation (20), the observable ϱ can be used to map temperature (Figure 2e). This approach is ratiometric and hence immune to factors such as fluctuations in the excitation, as well as photoinstability and inhomogeneous distribution of the molecules. However, it requires calibration as the temperature dependence is not as straightforward as Equation (20) might indicate. Alongside τ_R the viscosity μ and potentially also the fluorescent lifetime τ_F can depend on temperature. Optimization of the method can be achieved by controlling the viscosity μ and the hydrodynamic volume V in order to affect τ_R such that it is of the same order of magnitude of τ_F.[82] The technique relies on measuring the fluorescence anisotropy of an ensemble of molecules and has a spatial resolution given by the microscope (approximately diffraction limit). Temperature measurement employing this method have been carried out, for instance, using fluorescein molecules[30] (sensitivity ≈4–5% K^{-1}, over the range 293–343 K), and green-fluorescent protein in living organisms[83] (sensitivity ≈1% K^{-1}, over the range 297–308 K).

3.1.2. Benchmarking

Spatial Resolution: Organic dyes consist of molecules with sizes in the nanometer range. While the molecules themselves reach the nanoscale, most measurements are conducted on ensembles and, as the techniques are optical, their resolution is usually limited by diffraction.

Sensitivity[7]: The reported sensitivity of dye-based nanothermometers spans over the range ≈0.1–4.5% K^{-1} and while the fundamental mechanisms among the various methods might be quite different, many of the techniques are based on measuring changes in photoluminescence intensity—in many cases in ratiometric measurements.

Range[7]:]One of the main shortcomings of thermosensing techniques based on organic dyes is their limited operating range—a few tens of degrees around room temperature. Techniques using microencapsulation of the dye molecules in host matrices have however shown to work on greater ranges (e.g., 243–413 K).[74]

Utility: Organic dyes are very versatile. They are largely used in biological applications as they are bright, owing to a relatively high quantum yield, and can be functionalized to target different biomoieties, for instance within cells. With respect to nanothermometry, the number of organic dyes with thermosensing capability is large. Several molecular dyes are available commercially and can cater for specific experimental needs accounting for surface biochemistry and functionalization, as well as photo excitation/emission wavelengths—mainly in the UV–visible range, but with some options also in the near-IR spectral region.

Limitations and Sources of TEN: Organic dyes have some shortcomings that limit their use in practical realizations. One of the main drawbacks of some organic dyes is that temperature variations are mapped onto changes in the dye's photoluminescence intensity or lifetime. This means that experimental factors such as fluctuations of the excitation source, photobleaching of the dye—which is common in many organic fluorophores—variations of pH and inhomogeneous distribution of the dye can invalidate the measurement and are a potential source of TEN. This problem is severe, especially for environments (e.g., cells and tissues) that display light scattering and absorption, as well as considerable composition and refractive index inhomogeneities. This issue can be partially mitigated by means of ratiometric measurements: the signal from the thermosensing dye is normalized to that of a reference dye, which emits at a different wavelength and whose photoluminescence is independent of temperature. This has been achieved for instance by coupling the thermosensitive Rhodamine B with the reference dyes Rhodamine-110, Rhodamine-560, or Sulforhodamine-101.[84] However, absorption and scattering response of the environment might be wavelength-dependent, which means that even ratiometric measurement are not immune to TEN in practical realizations, when different wavelengths are used as signal and reference. Furthermore, even ratiometric methods still requires ensuring that the concentrations for the signal and the reference dyes are homogeneous, which can be achieved for instance by encapsulating both dyes in a (polymeric) nanoshell.[85] Excimer- and exciplex-based nanothermometers are self-referencing. They map temperature onto changes in photoluminescence intensity ratios between a temperature-dependent and temperature-independent signal, with emissions being, conveniently, at different wavelengths. Their use though still requires accounting for the possible wavelength-dependent response of the environment to avoid TEN.

The change in photoluminescence for some of these organic dyes depends on several factors other than temperature, e.g., changes in polarity, viscosity, or ionic strength of the surrounding medium as well as the concentration of other molecular species. While these effects can be controlled, for instance by encapsulating the dye in matrices of specific host materials, they require additional material synthesis and fabrication steps. To mitigate the effect of these parameters on TEN, an off- and in situ calibration is required. Another problem often overlooked in practical realizations relying on organic dyes is that of self-absorption. Due to the partial spectral overlap between the dyes' absorption and emission spectra, their photoluminescence emission spectra is red-shifted as emitted photons are self-absorbed by nearby dye molecules. Note that this effect increases with the concentration of the dye, which thus needs accounting for.

Finally, it should be noted that the temperature-dependent photoluminescence of organic dyes is often nonlinear with temperature—many processes show an Arrhenius-type relation. Linearity is not a strict requirement in nanothermometry, but it is something to consider as the nonlinearity leads to the sensitivity of the dye-nanothermometer being different depending on the operating range of temperatures.

3.2. Quantum Dots (QDs)

Semiconductor QDs are an obvious choice as candidate nanothermometers: they are small (size approximately nm) and display tunable and temperature-dependent photoluminescence. They are also resilient against photobleaching and, specific to biological applications, they display acceptable biocompatibility and biofunctionality after surface modification.[86]

3.2.1. Fundamental Mechanism(s)

Quantum dots are semiconductor nanoparticles whose electronic properties differ significantly from those of their bulk counterpart. As the size of the QD reduces to values comparable to the Bohr radius of the electron–hole bound state, quantum confinement of both the electron and hole wavefunctions leads to the discretization of the absorption and emission spectra and to an increase of the QD's effective bandgap relative to the bulk material. The absorption and luminescence of QDs can thus be tuned to specific photon energies by controlling their composition, size, and shape. This is attractive for photoluminescence-based nanothermometry as certain applications require specific wavelengths to operate effectively—e.g., within the biological window for biomedical applications.[87,88] From a practical standpoint, QDs are readily available and have been synthesized from many II–VI and III–V materials (e.g., ZnS, CdS, ZnSe, CdTe, and PbSe), with emissions ranging from the UV to the infrared (**Figure 3**a).[86,89–91] In nanothermometry, core–shell composite quantum dots (e.g., CdSe, Cds, and CdSeTe cores coated with ZnS shells) have found large applicability, as the higher bandgap inorganic shell produces desirable effects for (bio)sensing and (bio)imaging applications. For instance, it

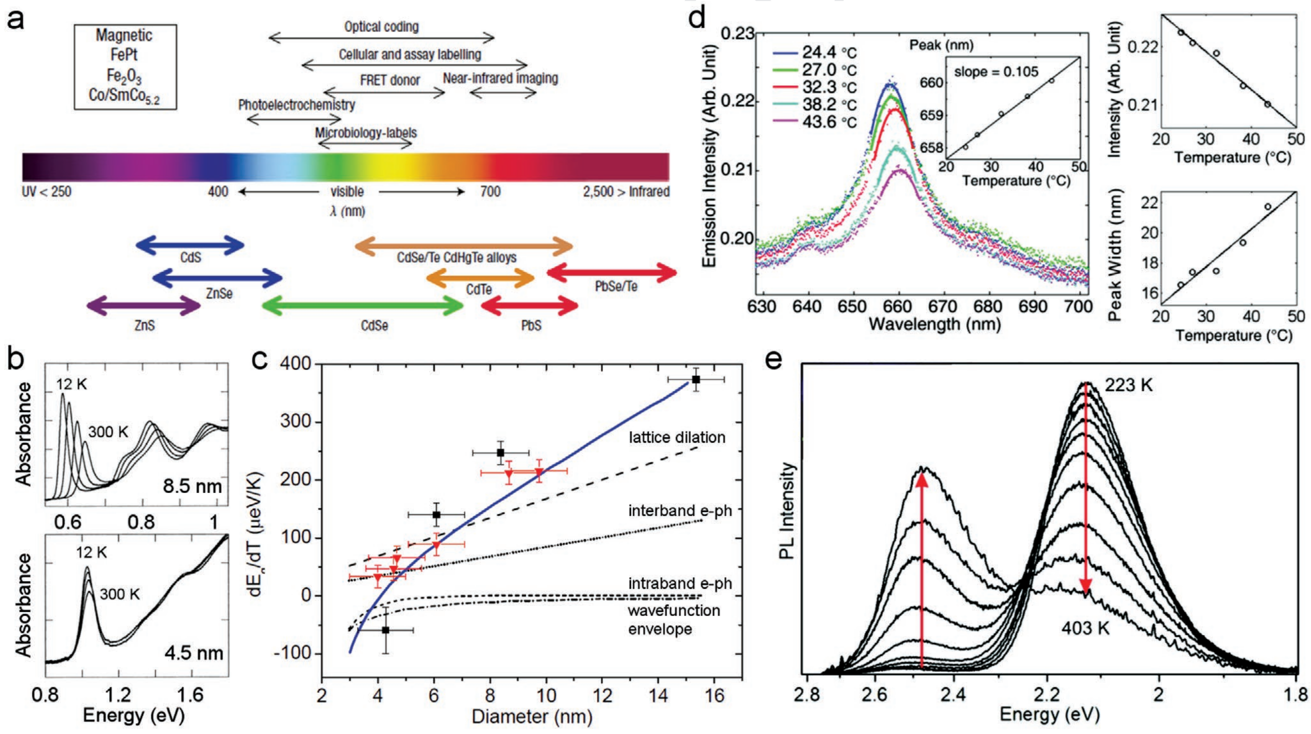

Figure 3. Fundamentals of quantum dots nanothermometry. a) Representative QD core materials organized by emission wavelength and relative to spectral region of interest for (bio)imaging and sensing. b) Absorption spectra of 8.5 and 4.5 nm PbS QD, recorded at 12, 100, 200, and 300 K. c) Relation dE_g/dT for PbS QD's. Calculated contributions to dE_g/dT are shown as dotted/dashed black lines, while the solid blue line is the sum of all contributions. Symbols are experimental values (black squares: phosphate glass host; red triangles: oxide glass host). d) Temperature-dependent spectral shifts of a single QD over the range 24.4–43.6 °C. The right panels show the average emission intensity (top) and the spectral linewidth variation (bottom) as a function of temperature. e) Temperature-dependent photoluminescence spectra of colloidal Zn$_{1-}$xMnxSe–ZnCdSe nanocrystals (core diameter ≈3.7 nm, shell thickness ≈0.4 nm) collected in 20 K intervals and normalized to total integrated intensity, showing intensity transfer between Mn^{2+} and excitonic bands as a function of temperature. a) Reproduced with permission.[89] Copyright 2005, Springer Nature. b,c) Adapted with permission.[92] Copyright 1998, American Physical Society. d) Reproduced with permission.[53] Copyright 2007, American Chemical Society. e) Adapted with permission.[35] Copyright 2010, American Chemical Society.

improves their radiative quantum yield by quenching surface nonradiative recombination processes—which is beneficial for increasing the signal-to-noise ratio of the photoluminescence-based temperature measurement. Additionally, the outer shell isolates the inner, often toxic, core—which is important in bioapplications, as well as for reducing photo-oxidative degradation.

For the purpose of thermosensing, temperature affects both the emission wavelength and the intensity of the QD's photoluminescence signal. It follows that either quantity can be used to monitor temperature variations in the QD's surroundings.

Wavelength Shift: The wavelength shift caused by temperature variations is usually different for different types of QDs depending on their type and intrinsic characteristics. Nevertheless, it is ultimately determined by the combination of a few temperature-dependent mechanisms that alter the energy gap E_g: lattice dilation, quantum confinement, mechanical strain, and electron–phonon coupling.[92–95] In bulk semiconductors, the dependence between the energy gap and temperature, dE_g/dT, is known experimentally[96,97] and has been extensively studied from a theoretical point of view.[98] The measured temperature dependence of energy bands (at constant pressure) is mainly due to the thermal expansion of the lattice and the renormalization of band energies by electron–phonon interactions.

$$E_g = E_0 - \alpha T^2/(T+\beta) \tag{21}$$

where E_g is the energy gap, which may be direct or indirect, E_0 is its value at 0 K, and α and β are constants. Theoretical analyses show that the temperature dependence in bulk semiconductors is such that $\Delta E_g \sim T^2$ for $T \ll \Theta_D$ and $\Delta E_g \sim T$ for $T \gg \Theta_D$, with Θ_D being the Debye temperature of the material.

However, size plays an important role and the relation dE_g/dT for a QD (E_g being the energy of the lowest exciton transition for QDs) can diverge significantly from bulk values—more than an order of magnitude in specific cases.[92] When the radius r of the QD is larger than the Bohr radius, r_B, of the electron–hole bound state, i.e., $r > r_B$, the values of dE_g/dT for QDs approach those for the bulk. However, when $r \leq r_B$, the energy E_g—and thus the related QD emission wavelength—becomes almost independent of temperature. This is mainly because in the strong quantum confinement regime ($r \leq r_B$), the energy levels of a QD are determined more by the size of the structure rather than by the lattice potential. Figure 3b highlights this size dependence in PbS quantum dots. Over the temperature range 12–300 K, the measured energy shift in absorption for 4.5 nm PbS quantum dots is much weaker (approximately tenfold) than that for the 8.5 nm ones, which show instead a dependence close to the bulk, $dE_g/dT \approx 500$ µeV K^{-1}. Besides being interesting from a fundamental point of view, this dependence makes size a crucial parameter in practical applications as it determines both the spatial resolution and the sensitivity of QD-nanothermometers based on photoluminescence wavelength shifts.

From a fundamental point of view, the dependence dE_g/dT for QDs—thus their variation in absorption and emission spectra—is dominated by two mechanisms: lattice dilation, $[dE_g/dT]_a$, and electron–phonon coupling, $[dE_g/dT]_{e-ph}$.[93] Other contributions include shifts of the quantum-confined energy levels due to thermal expansion, $[dE_g/dT]_{we}$, and due to mechanical strain and pressure from surface tension $[dE_g/dT]_s$.[99] The individual contributions to dE_g/dT for the representative case of PbS quantum dots are shown in Figure 3c as dotted/dashed black lines; their sum is shown as the solid blue line, and the experimental data is represented with red triangles and black squares.

For the lattice dilation contribution, $[dE_g/dT]_a$, variations in temperature alter the material lattice constant, a, effectively changing the bandgap energy

$$\left[\frac{\partial E_g}{\partial T}\right]_a = \frac{\partial E_g}{\partial a}\frac{\partial a}{\partial T} \tag{22}$$

As noted above, this effect diminishes as the size of the QD decreases, while it approaches bulk values for QDs' sizes $2r \sim r_B$.[100]

The effects of electron–phonon coupling on the QD's energy levels, term $[dE_g/dT]_{e-ph}$, can be calculated with perturbation theory.[101,102] In a QD the promotion of an electron from occupied to unoccupied levels results in a change of the self-energy ΔE

$$\Delta E = \sum_{l_p} \frac{\left|\left\langle n'^{(l'-l_p)}; l_p \middle| H_{e\text{-}ph} \middle| nl; 0 \right\rangle\right|^2}{E_{nl} - E_{n'(l'-l_p)} - \hbar\omega_p} \tag{23}$$

where l is the angular momentum of the electron, n represents all other quantum numbers for the electron, and l_p and ω_p are the angular momentum and frequency of the phonon. Thus ΔE is the result of intraband (coupling to like-carrier states) and interband (coupling to opposite-carrier states) contributions. The interband contributions decrease as the size of the QD decreases due to ΔE being inversely proportional to the spacing in energy between the quantum-confined energy levels (Equation (23)). The intraband self-energy is related to the electron–phonon coupling strength, S, and the Bose occupation factor, n_b

$$\frac{\Delta E}{dT} = -S(r)\langle\hbar\omega\rangle\frac{dn_b}{dT} \xrightarrow{T\to\infty} -S(r)k_B \tag{24}$$

As the temperature increases, the average energy and density of phononic states increases and so does the absolute value of electron–phonon coupling energy. Both coupling to optical phonons and deformation-potential coupling to acoustic phonons are present but for strong-confinements (i.e., small QD size), the deformation-potential coupling to acoustic modes dominates and produces a contribution linear with temperature to the self-energy ΔE.[103]

Other effects that contribute to dE_g/dT are shifts of the quantum-confined energy levels due to thermal expansion and mechanical strain, $[dE_g/dT]_{we}$ and $[dE_g/dT]_s$, respectively. The term $[dE_g/dT]_{we}$ can be determined as $(dE_g/dr)\alpha_L r$, with $\alpha_L = (1/r)(dr/dT)$ being the thermal expansion coefficient of the material, while the term $[dE_g/dT]_s$ can be estimated from the pressure coefficient of energy (dE_g/dP), which should vary negligibly with size from the bulk value.

Emission Linewidth: Alongside wavelength shifts, temperature also affects the FWHM, Γ, of the QD photoluminescence peak. Band-edge recombination of electron–hole pairs in QDs gives rise to a typical near Gaussian emission band[104] and, as the temperature increases, so does the linewidth (Figure 3d). There are two main mechanisms responsible for the linewidth change: inhomogeneous broadening—due to variations in size, shape, composition, etc., of the nanocrystals—and homogeneous broadening—due to scattering of the excitons by optical phonons and acoustic phonons[105,106]

$$\Gamma(T) = \Gamma_{\text{inh}} + \sigma T + \Gamma_{\text{LO}}\left(e^{E_{\text{LO}}/k_{\text{B}}T} - 1\right)^{-1} \tag{25}$$

where Γ_{inh} is the inhomogeneous broadening, σ is the exciton–acoustic phonon coupling coefficient, Γ_{LO} is the exciton–longitudinal optical (LO) phonon coupling coefficient, E_{LO} is the LO-phonon energy and k_{B} is the Boltzmann constant. The inhomogeneous contribution is independent of temperature while the homogeneous one depends on it and, as discussed above, is dominated at low temperatures by the excitons interaction with acoustic phonons.[94] Note that the coupling of excitons with acoustic phonons increases as the size of the QD decreases.[100,107] Also, coupling to dephasing process at the surface (e.g., surface defects or trap states) is possible, which can affect the homogeneous linewidth in the small size regime.[108] Figure 3d shows a representative temperature variation of the emission wavelength's FWHM for CdS QDs (≈7–12 nm, core–shell) over the range 24.4–43.6 °C.[32]

Emission Intensity: Alongside emission wavelength and linewidth, variations in temperature also drive changes in the luminescence intensity of QDs, with their emission becoming weaker as the temperature increases (Figure 3d). This phenomenon seems to be ubiquitous in QDs and has been attributed to the activation of phonon-assisted processes and thermally assisted energy transfer processes from bulk to surface (nonradiative) states.[33] Interestingly, this thermally induced luminescence quenching in QDs is linear at room temperature.[109,110] While not necessary, linearity is a desirable feature for thermal sensing for it ensures a constant sensitivity over the working temperature range of the nanothermometer.

Photoluminescence Lifetime: Temperature-driven changes in the emission intensity of QDs can be accompanied by corresponding changes in their lifetime. A raise in temperature usually leads to a decrease in the luminescence efficiency of the excitons due to the thermal activation of phonon-assisted electron–hole recombination. Simultaneously, as temperature increases, so does the probability of energy transfer from bulk excitons to nonradiative surface trap states.[111,112] Both mechanisms alter the relative contribution of radiative and nonradiative decay rates, which translates in an overall change in photoluminescence lifetime. Temperature measurements based on changes in lifetime have been realized using, for instance, CdTe and CdSe quantum dots.[36,113,114]

This analysis shows that QDs are strong nanothermometer candidates capable of mapping temperature onto variations of different experimental observables, e.g., photoluminescence wavelength, linewidth, and intensity. Yet, it also highlights that the temperature-to-observable mapping process is nontrivial. Several factors are at play simultaneously and their contribution can either be dominant or negligible at different size regimes. Notably, while independent studies on the same type of QDs report similar trends, the specific values of, for instance, dE_{g}/dT, can be different[92,115]—which indicates the temperature variation to be somewhat system-dependent. It follows that nanothermometry techniques based on monitoring the photoluminescence of QD-nanosensors require calibration curves specific for the type, characteristics and size of the QDs employed. Additionally, PL-based nanothermometry using QDs is not absolute. The PL detection can be affected by fluctuations of the excitation sources, absorption and scattering from the surrounding medium, as well as photoblinking of the QDs themselves. To mitigate these shortcomings, dual emission materials have been explored with the idea of normalizing the QDs PL to a reference signal. The measurement becomes ratiometric, thus immune to instabilities, as these affect both the measured signal as well as the reference, simultaneously. The first report of such an approach employed colloidal manganese-doped semiconductor $\text{Zn}_{1-x}\text{Mn}_x\text{Se}$–ZnCdSe core–shell QDs.[35] These nanocrystals show strong temperature-dependent luminescence involving two distinct but interconnected processes: the direct excitonic and the Mn^{2+} dopant ion emissions. The interdynamics between these two processes is thermally assisted; specifically, the relative intensity of the excitonic emission increases with temperature as population is transferred between the dopant and the excitonic states.[116] Figure 3e illustrates the method showing how temperature can be determined by measuring the temperature-dependent ratio between the excitonic (higher energies) and the Mn^{2+} (lower energies) emission intensities.

3.2.2. Benchmarking

Spatial Resolution: QDs can be as small as just a few nm, thus the sensors themselves reach the nanoscale size regime. However, most photoluminescence-based techniques are optical and thus diffraction-limited. This means that the spatial resolution of the measurement is of the order of the excitation wavelength—unless the nanosensor is isolated and its position with respect to the measured object can be known by more accurate means than optical imaging.

Sensitivity: The reported sensitivity of QD-based nanothermometer spans over the range 0.01–2.2% K^{-1},[33,117,118] with the highest sensitivity achieved by measuring changes in emission intensities in (CdSe)ZnS QDs, over the range 278–313 K.[119] It is worth pointing out that the thermal sensitivity (and stability) of QDs can be enhanced by design. This includes surface modification, e.g., with ligands,[95] as well as specific excitation/detection schemes, e.g., multiphoton fluorescence-imaging.[117,120]

Range: Techniques based on QDs are often characterized—owing to specific practical interest—in the vicinity of room temperature, or above. There are however several fundamental studies showing operating temperature as low as a few degrees K.[93,121]

Utility: Quantum dots are among some of the best developed temperature nanosensors. This stems from a series of characteristics that make them very flexible in terms of range of applicability. They display size-tunable absorption and emission wavelength, from the UV to the infrared, which makes them suitable for applications with specific wavelength requirements, e.g., in biomedical applications.[122–124] Quantum dots can be water-soluble and can be readily functionalized to target specific biomolecules[125,126]; they are also resistant to pH (5–7), ionic strength and other environmental variations.[127]

Limitations and Sources of TEN: Besides the standard limitations associated to photobleaching, photoblinking and—specific to bioapplications—possible long-term toxicity,[9,128,129] quantum dots possess a series of other aspects that need to be considered for use in nanothermometry. Similarly to organic dyes, they experience self-absorption, as their absorption and emission spectra partially overlap. This can cause both changes in photoluminescence emission intensity and wavelength—and thus temperature readings far from the true value. Note that self-absorption varies with the concentration of the luminescent QDs and must therefore be controlled during the course of the experiment.[130] Another possible cause of TEN is heating due to laser excitation and phonon-mediated nonradiative processes, which themselves are temperature-dependent as electron–phonon coupling increases with increasing temperature.

Furthermore, due to their small size—thus high surface-to-volume ratio—control experiments need to be carried out to ensure that when quenching is observed, it is due to temperature changes rather than chemical reactions occurring at the surface.[131] It should also be noted that intensity quenching can involve the escape of carriers to dark surface trap states, which has two associated issues. The thermal response of the QD intensity is surface/environment dependent, requiring calibration for each specific case. Also, for many QD systems thermal quenching has been found to be not fully reversible, causing repeatability and reliability concerns.[132]

Finally, general considerations apply to QDs as they do to other optical nanothermometers and must therefore be controlled for with specific calibration measurements. They include fluctuations in QDs concentration and in excitation power, as well as wavelength-dependent absorption and scattering of light by the surrounding environment.[9]

3.3. Upconversion Nanoparticles (UCNPs)

UCNPs are nanoscale particles that exhibit photon upconversion: their emission is at shorter wavelengths (e.g., visible) than their absorption (e.g., NIR). They are highly photostable, immune to bleaching, and show high signal-to-noise ratio—which is ideal for imaging biological samples due to the very low tissue autofluorescence.[133,134] Rare-earth ion doped upconverters operate via real, long-lived (approximately tens to hundreds of ms), intermediate states. The upconversion mechanism in UCNPs (**Figure 4**a) is based on either sequential excitation of the same emitting center in singly doped rare upconverters (addition de photon par transfert d'energie, APTE),[135] or via excitation of two centers and subsequent energy transfer in codoped rare-earth upconverters (energy transfer upconversion, ETU).[136–138] Fluorescence transition from the higher excited state to the ground state leads to fluorescence, which is observed as anti-Stokes emission. These properties make UCNPs ideal for 3D imaging and monitoring of biological processes over long time periods. Also, their imaging benefits from depth discrimination: the two-photon mechanism confines the focal volume to where the photon density is high and excludes fluorescence from regions outside it. The use of UCNPs as nanothermometers in 2D, in water has been demonstrated by Vetrone et al.[38] as well as others.[39] In general, the use of lanthanide-based materials for luminescent thermometry is well-established owing to their strong thermometric response and desirable (temperature-dependent) emission features.[139,140]

Both fluorescent dyes[29,80,84,141] and nanoparticles[110] are sensitive to local temperature changes and manifest this sensitivity through the change in their peak positions, relative peak intensities and lifetimes. Owing to their nonblinking[142] and nonbleaching properties, UCNPs allow for long term monitoring of the temperature changes in living systems, as opposed to for instance dye molecules, which are more prone to bleaching.

The nanothermometry capabilities of UCNPs are due to the emission of the Er^{3+} rare-earth ion,[143] specifically the intensity ratio of the $^2H_{11/2}$ to $^4I_{15/2}$ (525 nm) over $^4S_{3/2}$ to $^4I_{15/2}$ (545 nm) transitions, as shown in Figure 4a. The electrons in the 4f shell of rare earths are shielded from the surroundings by the filled 5s and 5p shells, and therefore the influence of the surrounding matrix on the optical transitions within the 4f shell is small, whether in crystals or in solution.

It follows that UCNPs display reduced sensitivity to physiological changes such as salt concentration[41] and pH while monitoring cellular temperatures.[144] UCNPs have also been used to measure the temperature of the interior nanoenvironment of magnetically heated iron oxide nanoparticles[145] and have been shown to enable direct measurement of the local temperature with high temporal (approximately ms) and thermal resolution (0.3–2.0 K),[42] as well as sensitivity (10^{-3}% K^{-1}),[146] all with simple equipment requirements. The emission of the dopant ions is sensitive to temperature in some configurations due to closely spaced energy levels being thermally coupled.[147,148] Moreover, these thermally coupled energy levels are not sensitive to other environmental factors such as scattering or tissue autofluorescence. Thermally coupled emissions, such as for the Er^{3+} rare-earth ion, can be in the visible, such as in the intensity ratio (RHS) of the $^2H_{11/2}$ to $^4I_{15/2}$ (525 nm) over $^4S_{3/2}$ to $^4I_{15/2}$ (545 nm) transitions[149] (Figure 4a), or in the red to near infrared, with the Tm^{3+} rare-earth ion, such as in the intensity ratio (RHS) of the $^3F_{2,3}$ to $^3H_6$ (700 nm) over the $^3H_4$ to $^3H_6$ (800 nm) transitions. The relative intensity of the two green bands can be understood by considering the energy separation between the nearest excited states Er: $^2H_{11/2}$ and Er: $^4S_{3/2}$, which is only several hundred wavenumbers. The population distribution on Er: $^2H_{11/2}$ and Er: $^4S_{3/2}$ should be dominated both by thermal distribution and nonradiative relaxation. The population of the Er: $^2H_{11/2}$ and $^4S_{3/2}$ levels varies as a function of the Boltzmann distribution. Measurements of the Boltzmann distribution between the two closely spaced states with varying temperatures show that the natural log of this ratio is inversely proportional to the temperature in the range relevant to most biological systems. Figure 4b, shows the dependence of the I_{525}/I_{545} ratio on temperature. The measurements show a predictable rise in the ratio as temperature increase, as well as that the ratios are independent of particle aggregation.

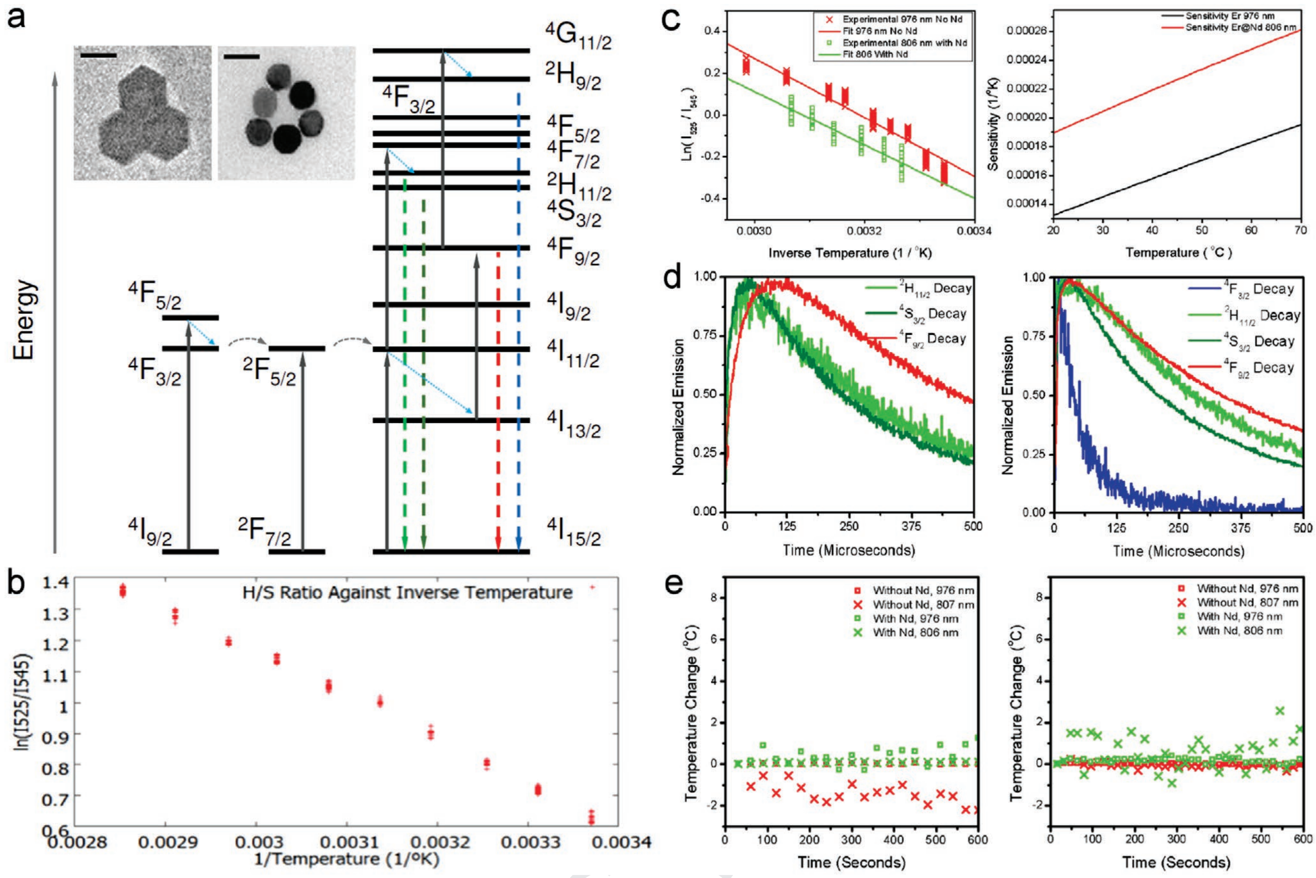

Figure 4. Fundamentals of UCNPs nanothermometry. a) Energy level diagram of the sensitization of erbium by neodymium and ytterbium at 806 and 976 nm excitation, respectively. Insets: transmission electron microscopy of both β-NaYF$_4$:20%Yb, 2%Er (top) and β-NaYF$_4$:40%Yb, 2%Er@NaYF$_4$:20%Yb@NaNdF$_4$:10%Yb particles (bottom). Scale bars are 100 nm. b) Plot of $\ln(I_{525}/I_{545})$ versus $1/T$. c) Experimental data for $\ln(I_{525}/I_{545})$ versus $1/T$ (left panel) for β-NaYF$_4$:20%Yb, 2%Er excited at 976 nm and β-NaYF$_4$:40%Yb, 2%Er@NaYF$_4$:20%Yb@NaNdF$_4$:10%Yb excited at 806 nm. The sensitivity over the working temperature range is plotted against temperature (right panel). d) Time-resolved decay for each of the visible emitting levels for β-NaYF$_4$:20%Yb, 2%Er at 1.0×10^4 W cm^{-2} (left panel) and 5.6×10^4 W cm^{-2} (right panel). The $^4F_{3/2}$ decay is only shown in the right panel where the measured intensity was sufficient to produce a readable signal. e) Plot of measured temperature converted from spectroscopic ratio against time at a fixed power for particles without Nd (β-NaYF$_4$:20% Yb^{3+}, 2%Er^{3+}) and with Nd (β-NaYF$_4$:40%Yb^{3+}, 2% Er^{3+}@NaYF$_4$:20%Yb^{3+}@NaNdF4:10%Yb^{3+}) in air (left panel) and in water (right panel). Powers used were 8.0×10^4 and 5.3×10^4 W cm^{-2} for 976 and 806 nm, respectively. Adapted with permission.[41] Copyright 2018, Frontiers Media S.A.

However, the primary excitation of the UCNPs occurs in the near infrared, where the absorption coefficient of water is high and can vary for different biological tissues, resulting in some reservations regarding the use of these nanoparticles as temperature sensors. Specifically, the absorption coefficient of water at 980 nm is about 20 times larger than that at 800 nm.[150] At 980 nm CW excitation, thermal heating of the biological environment, may hamper the measurement process, as seen in small animals, and in cellular systems. The more widely used sensitizer, the Yb^{3+} rare-earth ion absorbs primarily at 980 nm, corresponding to the $^2F_{7/2}$ to $^2F_{5/2}$ transition, whereas the Nd^{3+} rare-earth ion sensitizer absorbs at 800 nm, corresponding to the $^4I_{9/2}$ to $^4F_{5/2}$ transition. The Nd^{3+} ion has an absorption cross section one order of magnitude greater at 800 nm than the Yb^{3+} sensitizer.[150–152] Furthermore, infrared upconversion bioimaging at the molecular scale, occurs at a much higher intensity under a tightly focused excitation beam, and is normally coupled with pulsed excitation to provide higher peak powers, for sharper discrimination along the *z*-axis. Upconversion imaging is particularly suited to long-term single molecule imaging technology, that is resistant to photobleaching and is excited at longer wavelengths, which serves as a powerful tool to study physiological processes that take time to unfold, such as disease progression.

Figure 4c (left panel) shows a plot of $ln(I_{525}/I_{545})$ versus $1/T$ measured for both the β-NaYF$_4$:20%Yb, 2%Er UCNPs and β-NaYF$_4$:40%Yb, 2%Er@NaYF$_4$:20%Yb@NaNdF$_4$:10%Yb core–shell–shell UCNPs at 976 and 806 nm, respectively. Since the population of the Er: $^2H_{11/2}$ and Er: $^4S_{3/2}$ levels fluctuates as a function of the Boltzmann's distribution[148]

$$R = \frac{I_{525}}{I_{545}} = Ae^{-\frac{\Delta E}{k_B T}} \tag{26}$$

where by taking the slope of the $\ln(I_{525}/I_{545})$ versus $1/T$ plot, a ΔE of 887.170 cm^{-1} (806 nm, core–shell–shell with Nd) and 966.176 cm^{-1} (976 nm core only) is obtained (the pre-exponential factor A is derived from the fit). The calculated difference between the 545 and 525 nm peaks is 700 cm^{-1}. The absolute sensitivity S is defined as

$$S = \frac{dR}{dT} = A\frac{\Delta E}{k_B T^2} e^{-\frac{\Delta E}{k_B T}} \tag{27}$$

where the higher the temperature, the greater the sensitivity. Given the calculated ΔE, a plot of the sensitivity against temperature is shown in Figure 4c (right panel). The higher sensitivity expands the applicability to environmental and electronics sensing where typical critical operating temperatures are higher.

Figure 4d displays the decay spectra for $^4F_{3/2}$(blue), $^2H_{11/2}$(green), $^4S_{3/2}$(green), and $^4F_{9/2}$(red) emissions at two different excitation intensities. It can be seen that at a higher excitation intensity (5.6×10^4 W cm^{-2}) in Figure 4d (right panel), the $^4F_{9/2}$ and $^4S_{3/2}$ states excitation pathways are more strongly coupled as evidenced by the narrowing of the gap between their rise times (**Table 2**). This has been attributed to the increase in phonon coupling to the lattice OH vibrations at higher laser intensity. Therefore, excitation intensity is a parameter in upconversion nanoparticle nanothermometry that must be strongly controlled in order to avoid inadvertently affecting the I_{525}/I_{545} ratio, due to alteration of the optical pathways involved in ratio reporting.

For the temperature measurement to be accurate, the effect of the pump laser on local heating (due to the increased probability of higher energy level transitions) must be considered. Figure 4e shows the dependence of the local temperature with time duration of irradiation in air (Figure 4e, left panel) and water (Figure 4e, right panel), respectively.[41] Neither 976 nm, nor 806 nm excitation introduces a local temperature rise over time at laser intensities ≈10^4 W cm^{-2}. However, this is not always the case and is a direct consequence of using pulsed laser excitation. Previous studies where continuous excitation was employed reported local heating due to the pump laser.[150] Therefore, the laser mode of operation should be carefully considered when using upconversion nanocrystals for thermal sensing. While continuous wave lasers are affordable and highly adaptable to many laboratories, the probability of local heating is high. In contrast, pulsed wave excitation under a tightly focused beam, which is typical in single-molecule imaging, does not cause appreciable local temperature rise in the sample.

Q8 **Table 2.** Lifetime and rise time for β-NaYF$_4$:20% Yb^{3+}, 2% Er^{3+}.

	Blue[a)]	H	S	Red
5.6×10^4 W cm^{-2}				
Lifetime [µs]	53.792	352.113	267.308	432.339
Rise time [µs]	13.125	20.125	35.000	35.000
1.0×10^4 W cm^{-2}				
Lifetime [µs]	N/A	344.471	272.405	558.971
Rise Time [µs]	N/A	45.500	59.500	91.875

[a)] Lifetime and rise time were fitted from the time-resolved decay for β-NaYF$_4$:20% Yb^{3+}, 2% Er^{3+} from Figure 4d. The lifetime was fitted as a single exponential for the emission's decay and the rise time was defined as the time between the laser excitation and the maximum point of the decay curve.

Photoluminescence Lifetime

Besides fluorescence intensity ratios between different transitions, temperature also affects the lifetime of UCNPs. Albeit usually characterized by a lower sensitivity,[153,154] mapping temperature onto lifetime changes can be advantageous for a series of reasons. The method is for instance immune to inhomogeneities in the concentration of nanoparticles. It is also insensitive to scattering and absorption from the surrounding medium, which can be wavelength-dependent and can affect differently the collection of light of the different transitions. As mentioned before (cf. Section 3.1), it also potentially allows for shorter acquisition times avoiding the risk of local heating caused by the laser excitation. The change in the lifetime of UCNPs with temperature can be understood invoking phonon-mediated, nonradiative relaxation processes,[154,155] and can depend on the morphology and size of the nanoparticles. This is because, for instance, a higher surface-to-volume ratio would favor nonradiative transitions involving interactions with surface groups.[156] The total decay rate has both radiative and nonradiative components. The nonradiative one displays an Arrhenius-type behavior,[156] which allows using the lifetime of UCNPs as an observable to map the temperature of its surroundings. Lifetime-based thermometry utilizing UCNPs has been realized in several systems[139] including β-Na(Gd/Lu)F$_4$,[155] β-NaGdF$_4$:Yb^{c+}-Er^{3+},[156] Er:Yb:NaY$_2$F$_5$O,[153,157] YWO$_6$:Yb^{3+}-Er^{3+},[154] and CaLa$_2$ZnO$_5$:Er^{3+}-Yb^{3+},[158] to cite a few.

3.3.1. Benchmarking

Spatial Resolution: Upconversion nanoparticles can be synthesized down to sizes <10 nm.[159] However, the emission intensity is directly correlated to the total number of dopants, which makes smaller sizes impractical. Furthermore, due to the low absorption cross-section, the luminescence efficiency is relatively low compared to quantum dots and dyes. Larger particles, sizes >50 nm, are sufficiently bright to be imaged at the single particle level.[160]

Sensitivity: UCMP-based thermal sensing have been demonstrated at high temporal (approximately ms) and thermal resolution (0.3–2.0 K)[42] and sensitivity (10^{-5}% K^{-1})[146] with simple equipment requirements. Newer core–shell nanoparticles with higher luminescence efficiency,[41] are expected to enhance the sensitivity even further.

Range: While most studies have been focused on temperature mapping in biological systems at physiological temperatures, Dong and Zink, have demonstrated sensing over the range 295–973 K.[145]

Utility: Upconversion nanoparticles are uniquely suited for biomedical sensing due to their insensitivity to pH and salt concentration in the surrounding medium. However, the low luminescence efficiency and spectral changes with pump laser power, means that calibration is required. Also, while the infrared excitation is desirable to reduce background autofluorescence, it may lead to sample heating. Other infrared excitation wavelengths are thus currently explored, such as 800 and 915 nm,[161] or pulsed excitation applications.[122–124,162,163] While lanthanide doped UCNPs are basically considered as chemically nontoxic, toxicity due to nanoparticle size is a concern. It remains to be seen whether surface modification resulting in changes to the hydrodynamic size, surface charge and surface functional groups will remediate the toxicity issue.

Limitations and Sources of TEN: Upconversion nanoparticles are some of the most widely used nanothermometers. A recent report[25] however, has expressed concerns about their reliability as thermosensors due to often-overlooked artifacts that can lead to inaccurate temperature readings. A known issue is the dependence of the rare-earth ions' spectral emission on excitation power. This is especially relevant when UCNPs are used in complex biological media, and the environment's scattering, absorption, changes in refractive index, and deformation of the focal volume can result in excitation power densities much different from their nominal value. The problem can become hindering when the optical transitions used to estimate the temperature involve multiphoton absorption processes with different multiplicity.[164] For instance, the probabilities of two- and three-photon absorption have different power-law scaling with respect to the excitation power. If temperature is mapped onto the ratio of the corresponding emission peaks, a change in excitation power is phenomenologically indistinguishable from a change in temperature, and thus a cause of TEN.

Another factor is partial self-absorption due to the rare-earth ions having overlapping absorption and emission spectra. Quantifying the effect of self-absorption is nontrivial as it depends on the concentration and doping of the UCNPs, as well as other experimental conditions such as the optical path travelled by the emitted light through the UCNPs themselves. The surrounding environment plays again an important role as it can display wavelength-dependent absorption and scattering—not ideal when temperature is measured as ratio between different spectral lines from the UCNPs. This issue can however be partially mitigated by monitoring emission lines spectrally close to one other.

All these factors—excitation power, self-absorption and interaction with the environment—should be carefully controlled for, ideally with both off- and in situ calibrations, especially since they are strongly case-specific. Failure to control for these effects can lead to thermal equivalent noise up to several tens of degrees.[25]

3.4. Nanodiamonds

Nanodiamonds are nanoparticle or nanoscale bulk materials with linear size <100 nm. They can be host to complexes of foreign atom-like defects, which are known as color centers. Diamond color centers are attractive as, besides displaying photostable fluorescence, they are solid-state systems, which can retain their quantum spin-optical properties at room temperature. The most studied diamond color centers are the nitrogen-vacancy (NV) center[165] and the group IV (SiV, GeV, SnV, and PbV)[166] color centers. These have been successfully employed for quantum-enabled nanoscale sensing[167,168] and are an obvious choice for nanothermometry. Fluorescent nanodiamonds can emit light at different wavelengths and display temperature-dependent spin-optical properties, which allows for (parallel, multicolor) imaging and temperature monitoring. They are photostable up to several hundreds of K. They are nontoxic and can be functionalized to target specific biological moieties, which is attractive for sensing applications in biomedical settings.

3.4.1. Fundamental Mechanism(s)

The first proposals for diamond-based nanothermometers date back to 2010 and stemmed from the idea of mapping temperature variations onto changes in the luminescence and ground-state spin energy of the well-studied NV center.[169,170] For completeness, it should be noted that the temperature dependence of the NV's zero-phonon line (ZPL) energy and linewidth had already been investigated at the time of its first identification a few decades earlier.[171]

The NV center is an atom-like defect consisting of a substitutional nitrogen atom adjacent to a vacancy (i.e., a missing carbon atom) in the diamond matrix. The center has C_{3v} symmetry with the C_3 axis lying along the N–V direction. In its negatively charged state—i.e., upon trapping an additional electron from elsewhere in the lattice—the NV center displays triplet ground and excited states (**Figure 5**a). The ground triplet state, $^3A_2$, exhibits an axial zero-field fine splitting between the $m_s = 0$ and ±1 spin sublevels ($D_{gs} \approx 2.88$ GHz, at room temperature) mainly due to spin–spin interaction. The transverse zero-field splitting, E_{gs}, is zero for perfect C_{3v} symmetry making the +1 and −1 sublevels nominally degenerate. The excited spin triplet state, ^3E, is associated with a broadband photoluminescence emission with a ZPL wavelength at 637 nm. The excited state is an orbital doublet, in which degeneracy is lifted by nonaxial strain into two orbital branches with each orbital branch being formed by three spin states. Above 150 K, the fine structure of the ^3E excited state becomes analogous to that of the $^3A_2$ ground state with a zero-field splitting between the $m_s = 0$ and ±1 spin sublevels ($D_{es} \approx 1.42$ GHz, at room-temperature) and a strain-dependent splitting E_{es} of the $m_s = \pm 1$ sublevels. Figure 5a shows a simplified, working model for the NV energy level scheme where the ground and excited state triplets and the metastable singlets are displayed.

Notably, the spin of the ground state can be polarized, manipulated, and read out optically.[172]

Optical polarization: optical excitation from the ground to the excited state is spin conserving. Yet, as the NV decays from the excited to the ground state, spin-selective, nonradiative ISC through the metastable singlets competes with the spin-conserving, direct radiative decay. This process preferentially depopulates the ground $m_s = \pm 1$ sublevels and populates the $m_s = 0$ sublevel.

Manipulation: applying a microwave field resonant with the ground state axial zero-field splitting ($D_{gs} \approx 2.88$ GHz) allows for the manipulation of the ground state population by driving the $m_s = 0 \leftrightarrow \pm 1$ transitions.

Optical readout: as the $m_s = 0$ state scatters more photons than the ±1 ones, the spin state population of the ground level can be detected through optically detected magnetic resonance

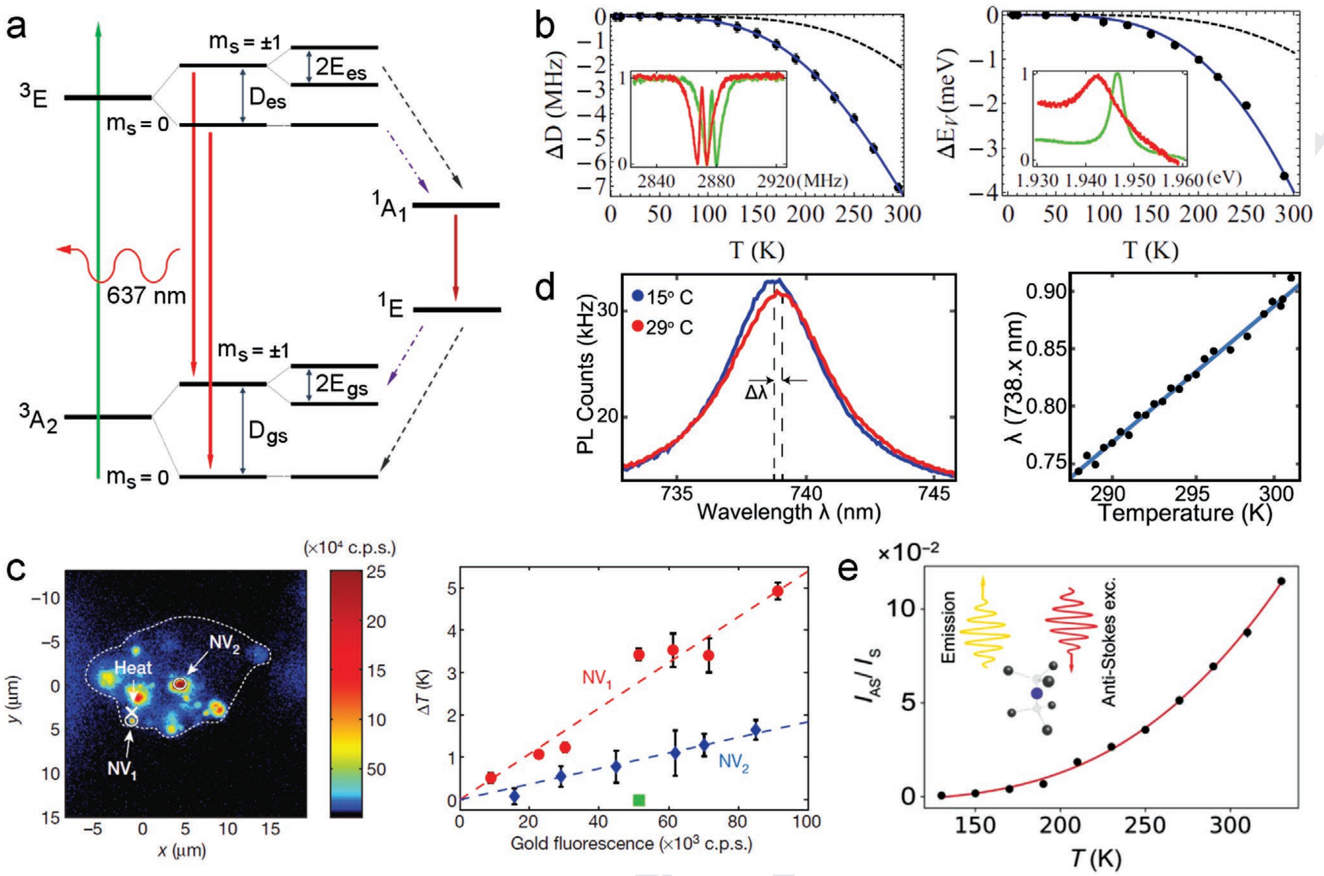

Figure 5. Fundamentals of diamond-based nanothermometry. a) Simplified energy level scheme of the diamond nitrogen-vacancy (NV) center. b) Temperature shifts of the NV⁻ spin (ΔD_{gs}, left panel) and visible (ΔE_V, right panel) resonances [black points: measurements; blue curves: fit obtained using Equation (32)]. The contributions of thermal expansion $E_{ex}(T)$ to each shift alone are depicted as dashed black curves. Insets: example ODMR (left) and photoluminescence spectra (right) of the resonances at 5 K [green] and room temperature [red]. Reproduced with permission.[174] Copyright 2014, American Physical Society. c) Left: confocal scan of a single cell. The cross marks the position of a gold nanoparticle excited by the laser to heat its surroundings; the circles represent the location of two nanodiamonds (NV1 and NV2) used for thermometry. Right: measured change in temperature at the positions of NV1 and NV2 relative to the incident laser power applied to the gold nanoparticle. Reproduced with permission.[22] Copyright 2013, Springer Nature. d) Left: spectra at 15 °C (blue) and 29 °C (red) of SiV centers in diamond. The ZPL peak red-shifts as the temperature increases. Right: peak position as a function of temperature. Reproduced with permission.[45] Copyright 2018, American Institute of Physics (AIP). e) Temperature dependence of the ratio (I_{AS}/I_S) between the PL intensity of GeV centers in a nanodiamond under anti-Stokes and Stokes excitations. Adapted with permission.[23] Copyright 2019, American Association for the Advancement of Science.

(ODMR)—a drop in fluorescence of up to ≈30% is observed when the system is in the $m_s = \pm 1$ states rather than in the $m_s = 0$ one. Furthermore, in the presence of an applied magnetic field, B, the $m_s = \pm 1$ levels split, displaying resonances separated by $2g_{NV}\mu_B$, where $g_{NV} = 2003$ is the NV Lande factor and μ_B is the Bohr magneton. Note that local strain (thus pressure and temperature) can also lift the $m_s = \pm 1$ degeneracy.[172]

As the temperature varies, the NV center undergoes a series of changes including in fluorescence intensity, ZPL wavelength barycenter and linewidth, as well as changes in the axial, D_{gs}, and the transversal, E_{gs}, zero-field splitting energies. Any of these quantities can thus be used to map temperature values.

Photoluminescence Intensity: One of the first demonstrations of diamond-based nanothermometry, exploited the dependence of the NV center PL intensity on temperature.[169] In the experiment, the PL emission intensity of NV centers hosted in diamond nanoparticles (size ≤35 nm) was found to decrease up to fourfold as temperature increases over the range 320–670 K. A 2.7-fold reduction in PL lifetime was also reported leading to the possibility of measuring the temperature of the diamond nanoparticles and their surroundings by monitoring either of these quantities.

The drop in PL intensity as temperature increases is explained invoking the breakdown of the NV optical polarization mechanism (cf. optical polarization above). Optical excitation of the NV center preferentially depopulates the ground $m_s = \pm 1$ sublevels and populates the $m_s = 0$ sublevel which, upon laser excitation, scatters more photons than the $m_s = \pm 1$ sublevel (the intersystem crossing rate from the excited $m_s = 0$ state to the metastable singlets is 10^{-4} times that from the $m_s = \pm 1$ states).[165] As the temperature increases, the spin–lattice relaxation rate increases (this rate equals 2 Hz at 100 K and 1 kHz at 300 K) and as a consequence the population of all triplet sublevels equilibrates. This effectively neutralizes the optical polarization mechanism of the center, subsequently reducing—in a nontrivial manner—its photoluminescence.

As expected, the relative change of the radiative and nonradiative rates also results in a corresponding change in PL lifetime.[169] However, it should be noted that these temperature-dependent variations in PL intensity and lifetime were found to differ dramatically from nanodiamond to nanodiamond requiring calibration of each nanocrystal against a known set of temperatures prior to their practical use. Also, the PL intensity measurement is nonratiometric, which implies that light absorption or scattering from the surrounding medium might hinder the accuracy of the temperature reading and hence the utility of the method. In 2015, a refined technique for measuring temperature by monitoring the amplitude of the NV center's ZPL was demonstrated.[43] The technique relies on measuring the ratio between the amplitude of the NV's ZPL and the value of the background fluorescence at the NV's ZPL wavelength. The latter involves vibrational excitations in the NV's excited state, which obey temperature-dependent Boltzmann statistics and can be accurately modeled semiempirically. While several quantities—specifically ZPL amplitude, linewidth and Debye–Waller factor (DWF, i.e., the ZPL area divided by the total area of the spectrum) depend on temperature (see below), the aforementioned amplitude ratio has a larger temperature sensitivity than both DWF and linewidth.[173] The method was shown to achieve a noise-floor temperature resolution of 0.3 kHz K^{-1}.

In the context of nanodiamond-based thermometry, photoluminescence intensity measurements are often employed in combination with other quantities to measure temperature (see below).

Spectral Shift: The effects of pressure and temperature on the energy levels of the NV center—thus on its visible and infrared ZPL emissions—have been studied in depth.[174–176] For diamond color centers, there are two main contributions to the temperature shift in the ZPL energy. 1) Strain caused by thermal expansion/contraction perturbs the electronic energies of the atom-like defect. 2) The vibrational frequencies of the electronic levels change as the potential energy functions (curvature) of the electronic levels vary. This can be equivalently described as outcome of quadratic electron–phonon interaction.

As temperature varies, so does the relative distance between the equilibrium positions of the nuclei and the associated energy of the electronic levels. Accordingly, all the zero-phonon transition energies shift, which results in the observation of a shift in ZPL energy $\Delta E_{\mathrm{ex}}(T)$—as thermal average of all zero-phonon transitions[43]

$$\Delta E_{\mathrm{ex}}(T) = \left.\frac{\partial \Delta E_{\mathrm{el}}}{\partial \Delta Q_{\mathrm{ex}}}\right|_0 Q_{\mathrm{ex}}(T) \tag{28}$$

In Equation (28), $Q_{\mathrm{ex}}(T)$ is the mass-weighted nuclear displacement coordinate of thermal expansion, $\Delta E_{\mathrm{el}} = (E_{\mathrm{el},i} - E_{\mathrm{el},j})$ is the difference in energy between the ith and the jth electronic states and the derivative is calculated at $Q_{\mathrm{ex}} = 0$. Since thermal expansion and hydrostatic pressure are related, Equation (28) can be rewritten in a more compact form

$$\Delta E_{\mathrm{ex}}(T) = AP(T) \tag{29}$$

where $A = 14.58(6)$ MHz GPa^{-1} is the hydrostatic pressure shift of the ZPL and $P(T) = B\int_0^T e(t)\mathrm{d}t$ is the pressure of thermal expansion; $B = 442$ GPa is the bulk modulus of diamond and $e(T)$ is the diamond volume expansion coefficient.

The energy of a zero-phonon transition also depends on the vibrational density of modes, $\rho(\omega)$, and the Bose-Einstein thermal distribution of vibrational occupation $n(\omega,T) = 1/(\mathrm{e}^{\hbar\omega/k_{\mathrm{B}}T} - 1)$, specifically

$$\Delta E_{\mathrm{e-p}}(T) = \hbar\int_0^{\Omega} n(\omega,T)\delta(\omega)\rho(\omega)\mathrm{d}\omega \tag{30}$$

where $\Omega \approx 165$ meV is the highest vibrational frequency of diamond and $\delta(\omega)$ is the average vibrational frequency difference between the electronic states, which is defined by

$$\delta(\omega)\rho(\omega) = \sum\nolimits_{\alpha:\omega_{1,\alpha}=\omega}(\omega_{1,\alpha} - \omega_{2,\alpha}) \approx \frac{1}{2\omega}\sum\nolimits_{\alpha:\omega_{1,\alpha}=\omega}\left.\frac{\partial^2 \Delta E_{\mathrm{el}}}{\partial Q_{\alpha}^2}\right|_0 \tag{31}$$

In Equation (31), Q_{a} and $\omega_{i,\alpha}$ are the mass-weighted displacement coordinate and frequency of the αth mode in the ith electronic state, respectively. The derivative is evaluated at $Q_{\mathrm{a}} = 0$ and the sum is over all modes with frequency $\omega_{i,\alpha} = \omega$.

The total ZPL shift is thus $\Delta E(T) = -\Delta E_{\mathrm{ex}}(T) - \Delta E_{\mathrm{e-p}}(T)$. The quantity $\Delta E_{\mathrm{ex}}(T)$ can be determined[172] using the known values for the NV$^-$ hydrostatic pressure shifts A and the volume thermal expansion coefficient of diamond $e(T)$ (note that $e(T)$ varies with the purity of the diamond sample). The quantity $\Delta E_{\mathrm{e-p}}(T)$ can be approximated[174] to $\Delta E_{\mathrm{e-p}}(T) \approx \sum\nolimits_{i=4} b_i T^i$, which produces the following expression for $\Delta E(T)$ (terminating the expansion at T^5)

$$\Delta E \approx -\frac{e_1}{2}ABT^2 - \frac{e_2}{3}ABT^3 - \left(b_4 + \frac{e_3}{4}AB\right)T^4 - \left(b_5 + \frac{e_4}{5}AB\right)T^5 \tag{32}$$

Interestingly, the parameters of $\Delta E_{\mathrm{e-p}}(T)$ are an order of magnitude larger than those of $\Delta E_{\mathrm{ex}}(T)$, at their respective powers of T. This reveals the importance of electron–phonon interactions in determining the energy shifts.[174] Figure 5b (right panel) shows the shifts of the NV$^-$ visible ZPL (ΔE_{V}) resonance as a function of temperature. With reference to Figure 5a, note that the model can be applied specifically to determine the temperature dependence of D_{gs}, E_{gs}, and D_{es} and E_{es} by determining the corresponding expressions for $\Delta D_{\mathrm{gs}}(T)$, $\Delta E_{\mathrm{gs}}(T)$, and $\Delta D_{\mathrm{es}}(T)$, $\Delta E_{\mathrm{es}}(T)$—the parameters A_{gs}, A_{es}, and $\delta_{\mathrm{gs}}(\omega)$, $\delta_{\mathrm{es}}(\omega)$ can be obtained from first-principles.[173] Figure 5b (left panel) shows the temperature dependence of the NV$^-$ center's D_{gs} through monitoring the shift in frequency of the spin transitions $m_{\mathrm{s}} = 0 \leftrightarrow \pm 1$ in a ODMR measurement.

ZPL Width: For color centers in crystalline hosts, the ZPL linewidth in the emission spectrum displays a temperature-dependent broadening, which can be both inhomogeneous and homogeneous in nature.

One of the main mechanisms responsible for the inhomogeneous broadening of the ZPL is spectral diffusion. Spectral diffusion occurs due to charge fluctuations in the local environment surrounding the defects. It produces a Gaussian profile for the center's ZPL, which can vary with temperature if the dynamics of these charge fluctuations is thermally activated.[177]

The homogeneous broadening is instead due to dephasing of the center's electronic state caused by quadratic electron–phonon coupling. It depends both on the spectrum and population of the phonon modes of the crystalline host surrounding the defect and is associated with a Lorentzian lineshape.[178,179] For temperatures T below the Debye temperature, Θ_D, the centers' ZPL linewidth, γ, is expected to display a dependence $\gamma \sim T^7$, at least in the ideal case in which only nondegenerate electronic states are involved in the transition (in diamond $\Theta_D \approx 2 \times 10^3$ K). However, in different experimental studies the ZPL linewidth of diamond NV centers has been found to show broadening captured by the polynomial relation $aT^3 + bT^5 + cT^7$ (with a, b, and c constants) where the weight of the T^3, T^5, or T^7 dependency varied significantly from study to study.[180,181] The T^3 behavior has been attributed to different mechanisms. These include: i) involvement of degenerate electronic states and ii) the decrease in bond strength as temperature rises leading to an increased density of low-energy local phonons in the excited state of the color center, as well as iii) fluctuating fields originating as phonons modulate the distance between the color center and other defects in the crystal (this effect would show dependence on the purity of the sample).[182] Using perturbation theory, the T^5 dependence of the ZPL linewidth at low temperature has instead been attributed to transitions between different components of the degenerate state following phonon scattering (dynamic Jahn–Teller effect).

From this analysis, it follows that methods based on mapping temperature onto the ZPL linewidth of diamond color centers require calibration against a reference set of temperatures, possibly specific to each nanoparticle host.

Spin-Resonances: The nitrogen-vacancy center has spin-dependent photoluminescence (cf. optical polarization, manipulation, and optical readout above), which allows sensing schemes based on monitoring shifts in the spin resonance frequencies (i.e., shift in the $m_s = 0 \leftrightarrow \pm 1$ transitions) through the defect's fluorescence as a function of external perturbations including magnetic and electric fields, as well as temperature.[172,183]

With reference to Figure 5a, the crystal field parameter D_{gs} depends on temperature, axial electric field and strain; the transverse ZFS parameter E_{gs} is nominally equal to zero but can be nonzero due to local strain. This means that in the absence of external magnetic and electric fields it is possible to map temperature changes onto relative energy shifts between the $m_s = 0$ and ± 1 ground sublevels of the NV center. It is important to note that the suppression of local electric and magnetic fields is nontrivial. The NV center is an atom-like system in a solid-state host and its energy can be affected by axial electric fields due to lattice defects and axial magnetic interactions with, for example, spin impurities. To isolate the contribution of temperature on D_{gs} and E_{gs} from those due to local fields, specific sequences involving laser, microwave, and radio-frequency pulses have been developed.[184] From a practical point of view, the measurement of the energy shifts is carried out optically by detecting drop in photoluminescence intensity (cf. optical readout) as the microwave field becomes resonant with the $m_s = 0 \leftrightarrow \pm 1$ transition frequencies. Over the temperature range 280–330 K it was empirically found that $\mathrm{d}E_{gs}/\mathrm{d}T = -0.4(2)$ kHz K^{-1} and $\mathrm{d}D_{gs}/\mathrm{d}T = -74.2(7)$ kHz K^{-1} (this corresponds to a sensitivity of $2.59(2) \times 10^{-3}$% K^{-1}). The trend of D_{gs} with temperature has been explained using a model based primarily on the thermal expansion of the crystal lattice. According to the model, the effect of lattice expansion on D_{gs} is[170]

$$\frac{1}{D_{gs}}\frac{\mathrm{d}D_{gs}}{\mathrm{d}T} \approx \frac{1}{D_{gs}}\frac{\mathrm{d}\left\langle \left(r_{12}^2 - 3z_{12}^2\right)/r_{12}^5\right\rangle}{\mathrm{d}R}\frac{\mathrm{d}R}{\mathrm{d}T} \qquad (33)$$

where r_{12} is the displacement between the two spins z_{12} is the component of r_{12} along the NV symmetry axis, and R is the distance between two basal carbon nuclei. This model is only partially successful and a more accurate dependence of D_{gs} on temperature likely requires considering additional vibronic effects.

The practical use of the NV spin-resonances to measure temperature at the nanoscale has been successfully realized in 2013.[21,22] The method demonstrated achievable resolutions of 1.8 mK Hz$^{-1/2}$ in a pure bulk diamond crystal and 200 mK Hz$^{-1/2}$ in nanodiamonds having a spatial resolution of 200 nm in living cells.[22] Figure 5c shows these results. Two nanodiamonds containing NV centers were placed inside a living cell and used to measure local changes in temperature as an incident laser heated up gold nanoparticles in the nanodiamonds surrounding.

Group IV Color Centers: Diamond-based nanothermometry has been explored using color centers in diamond other than the NV center, specifically the so-called group IV emitters. These are atom-like complexes hosted in the diamond matrix and consisting of an atom from the group IV column of the periodic table (Si, Ge, Sn, and Pb) located in between two missing carbon atoms (vacancies) in a split-vacancy configuration.[166] The nanothermometry techniques developed using nanodiamonds hosting these color centers are mainly all-optical methods. They are based on monitoring temperature-dependent changes in photoluminescence intensity, as well as position and linewidth of the center's ZPL wavelength.

While there is a strong parallelism between group IV emitters and NV centers regarding the nature of the temperature dependence of these quantities, there are also some differences. For instance, the shift and broadening of the spectral lines of SiV and GeV centers are mainly due to second- and first-order electron–phonon interaction in the excited state. The electron–phonon interaction rate is much higher than the spontaneous decay rate resulting in the strong temperature-dependent modification of the linewidth and position of the emission wavelength. A characteristic T^3 dependence of the zero-phonon line position is observed for SiV and GeV centers (above specific thresholds temperatures) as two-phonon processes dominate over single-phonon processes.[185,44] These specificities lead to the magnitude, and thus the sensitivity, of each method to be color-center specific. Nanothermometry techniques using silicon-vacancy (SiV),[24,45] germanium-vacancy (GeV),[44] and tin-vacancy (SnV),[46] centers are all well established. Figure 5d shows the representative example of the SiV center: spectra recorded at 288 and 302 K reveal that the ZPL peak shifts to longer wavelengths as temperature increases.

Interestingly, a multiparametric analysis scheme has been recently proposed to increase the resolution/speed of PL-based temperature measurements.[24] The scheme is mentioned here as its effectiveness—a tenfold improvement in resolution/speed—has been demonstrated by measuring temperature via the PL signal of diamond SiV centers. Note however that the scheme is not restricted to diamond color centers and could be implemented in other systems. In the demonstration, an overall 10^3-fold improvement is reported but the multiparametric method only accounts for a factor 10. Briefly, rather than monitoring one specific physical quantity—e.g., ZPL intensity, linewidth, wavelength, etc.—the proposed scheme monitors a set of them and assigns weights to each quantity to minimize noise. The multiparametric analysis improves the resolution by improving the signal-to-noise ratio of the measurement; or equivalently, it reduces the acquisition time for a fixed precision in resolution.

Also recently, an original diamond-based nanothermometry approach has been proposed. The method is based on measuring the PL intensity of diamond color centers under anti-Stokes excitation.[23] The method relies on exciting, optically, the color centers with a laser at longer wavelengths (lower energies) than the centers' emission ZPL. The extra (missing) energy that causes upconversion of the photons is acquired by absorption of phonon(s) with an efficiency that depends on the phonon spectral density, i.e., the phonon density of states multiplied by the transition amplitude. The resulting intensity of the emission exhibits an Arrhenius-type exponential scaling with temperature, $\approx A e^{-(E_a/k_B T)}$, with k_B being the Boltzmann constant, E_a the value for the activation energy fixed at the difference in energy between the anti-Stokes excitation laser and the color centers' ZPL, and A the amplitude fitting constant. To make the measurement ratiometric (Figure 5e), the anti-Stokes PL emission is normalized to the PL emission obtained under traditional Stokes excitation at shorter wavelengths (higher energies). The exponential dependence of the anti-Stokes excitation mechanism with temperature results in a relatively highly sensitivity, $\approx 1.3\%\ \mathrm{K}^{-1}$ (at 300 K), which is comparable or slightly higher than conventional Raman-based temperature measurements, yet with a much higher spatial resolution (set by the diffraction limit of the detection system).

3.4.2. Benchmarking

Spatial Resolution: Fluorescent NDs containing color centers can be of any size ≥5 nm. Note that the number of color centers, thus the corresponding PL intensity, scales with the volume of the particle, which means that NDs can be tailored to meet ad-hoc, application-specific requirements. As per other nanoparticle-based sensing techniques the spatial resolution of the measurement is set by the diffraction limit of the detection apparatus, unless the position of the nanosensor is established by more accurate means.

Sensitivity: The reported sensitivity of ND-based nanothermometer spans over the range 0.0015–1.3% K^{-1}. Nanodiamond-based thermometry has also been shown[23] to achieve some of the highest noise-floor temperature resolutions ≈1.8 mK $\mathrm{Hz}^{-1/2}$.

Range[23]: Nanodiamond-based techniques are among the more versatile in terms of range. In fact, diamond and its hosted fluorescent color centers are stable to up to 1000 K. From a practical point of view though, due to such a large range, at different temperatures certain mechanisms might become dominant or negligible over others for determining the temperature dependence of an observable. Calibration of the nanothermometer is thus necessary in most cases.

Utility: Nanodiamonds rank highly in overall utility. The variety of color centers the diamond matrix can host results in the NDs being capable of absorbing/emitting over a large portion of the spectrum, from the visible to the near infrared.[186] Notably different color centers can coexist in the same nanoparticle allowing for parallel, multicolor imaging and temperature sensing. Nanodiamonds are nontoxic, they are generally chemically inert and thus robust against changes in the local chemical environment, but they can also be readily functionalized to a large range of target-specific biomoieties,[187] which makes them ideal for biomedical applications. Simultaneously, nanodiamonds can resist harsh environments, which is crucial for certain applications such as monitoring temperature in high-power electronics.[1]

Limitations and Sources of TEN: Diamond-based nanothermometers suffer from the same general limitations discussed at length for other nanothermometers (e.g., wavelength-dependent absorption and scattering from the surrounding environment and fluctuations in laser excitation power), as well as some specific ones.

They are for instance subject to self-absorption and the associated changes in photoluminescence emission intensity and wavelength. It should be noted however that some diamond-based thermometry schemes can rely on collecting the photoluminescence signal from individual, single-photon emitters[22,23]; and are therefore immune to the problem.

Another factor to consider is heating of the diamond nanoprobe, either due to laser excitation or to phonon-mediated nonradiative processes. These problems are not unique to diamond nanothermometers and have already been discussed. We specifically mention them here because in nanodiamonds they have been studied in detail in optical levitation experiments, where absorption of the excitation laser from diamond impurities and surface carbon has been found to cause graphitization and burning of the diamond nanoparticles themselves.[188] While the laser powers used in these levitation experiments far exceed (by several orders of magnitude) those used in nanothermometry applications, the same absorption mechanisms could cause local thermal heating of the diamond probe and must therefore be considered for TEN. Related to thermal heating is also the fact that methods based on reading out the spin state of diamond NV centers rely on microwave excitation,[21,22,174] which is readily absorbed in biological environments and can be a source of error. Furthermore, methods based on the NV spin read out cannot determine whether the measured energy shift in the ground spin sublevels is due to temperature changes or to variations in local electric/magnetic fields. This is another potential source of TEN especially in biological environments where local fluctuating electric and magnetic fields are present and can mimic temperature effects.[189,190] Note that separating the effects of temperature and local fields is possible, but requires advanced experimental procedures.[21] It should also be emphasized that these issues only apply to methods based on the spin readout of diamond NV centers.

Finally, similarly to QDs, nanodiamonds can be very small (approximately a few nm). In thermometry applications, control experiments (e.g., off- and in situ) should therefore be carried out to separate between photoluminescence changes due to temperature variations and those due to interaction with surface ligands, surfactants and trap states.

4. Selected Applications

4.1. Biological and Medical Applications

Nanothermometry finds most of its application in biomedicine. Here, one of the key challenges is overcoming light scattering and absorption of the biological medium, which can affect the resolution of many of the nanoscale thermosensing techniques. Over the past few decades, various types of temperature sensors operating in the first and second biological windows, BW-I (700–950 nm) and BW-II (1000–1350 nm), have been developed for use in life science. Biothermometry can be classified into three categories based on the systems under investigation: a) subcellular, b) cellular, and c) tissue. A number of comprehensive review articles are already available in the literature on these research topics.[10,11,191–193] We summarize the recent advancements (mostly for the period 2016–present) and briefly discuss some salient examples of these three classes of thermometry.

4.1.1. Subcellular Thermometry

Measuring intracellular temperature is a topic of intensive investigation in biophysics for it can help elucidate the dynamics of target metabolic processes inside living cells. The types of nanothermometers employed in this context include organic dyes,[194] fluorescent proteins,[195,196] polymers,[197] and inorganic nanoparticles[198–204] (cf. Sections 3.1–3.4). Dye-based fluorescent probes are often employed for targeted imaging and temperature sensing of mitochondria—the source of biological energy generation within cells. However, due to rapid photobleaching of the dyes, temperature measurement with individual molecules is not possible. Similar problems also affect fluorescent proteins, which are nonetheless desirable thanks to their ability to be genetically engineered to label specific biotargets. Conversely, inorganic nanoparticles, e.g., rare-earth-doped nanoparticles[198] and fluorescent nanodiamonds,[199–204] are considerably more photostable even under extensive laser excitation. They can thus be observed individually in living cells over extended periods of time. Nevertheless, one of the major drawbacks that limits their use for nanothermometry, is their inability to directly target specific biomolecules and organelles. Specific targeting is indeed possible but requires an additional step involving chemical modification of the nanoparticles' surfaces, inevitably limiting their utility (cf. Section 2.2.5). The spatial resolution achieved so far by temperature sensing techniques based on single-particle nanothermometers is ≈200 nm.[22] This is set by the diffraction limit of light, as many of these techniques rely on collection of photoluminescence in this spectral region through an optical system. Subdiffraction resolution is however possible if other microscopy techniques are used in parallel, e.g., super-resolution fluorescence microscopy.

Recently, fluorescent carbon nanoparticles—nanodiamonds[199–204] and carbon dots[205,206]—have been explored as suitable and promising nanosensors for thermometry. These nanoparticles are appealing for their inherent biocompatibility, low cyto-toxicity, and high photostability. In this regard, fluorescent nanodiamonds are particularly attractive for subcellular temperature sensing as each nanoparticle can contain bright ensembles of color centers, which can be readily imaged at the single-particle level by standard confocal microscopy. The nanodiamonds can be engineered to host one or more types of color centers—consisting of different complexes of atom-like defects—which allows for wavelength tunability as well as parallel, multicolor imaging. While less versatile in this respect, carbon dots are comparatively more useful for ensemble temperature measurement of entire cells due to their smaller sizes. Some of the most successful thermosensing applications employing nanodiamonds include determining the local thermostability of cell membrane and monitoring the local temperature of a living cell as laser-induced heating was taking place at sites of interest. For instance, Tsai et al.[199] conjugated 100 nm fluorescent nanodiamonds to gold nanorods through non-covalent interactions. These two-in-one nanohybrids were then deposited on the plasma membrane of a cell cluster derived from the human embryonic kidney cell line (HEK293T), as shown in **Figure 6**a,b. A single laser (594 nm) was employed both for heating and for monitoring the temperature of these ad-hoc-designed nanohybrids inside the cells or onto the cells' membrane. They were able to determine that a local temperature of up to 333 K was necessary to rupture the membrane of the human cells under study. By extension, all-optical methods of this nature can be used to measure and control (usually increase) the temperature of a living organism both at the intra- and intercellular level—provided that the absorption and scattering of the biological environment allows for the detection of the optical signal through the tissues.

4.1.2. Cellular Thermometry

On a larger scale, temperature sensing of whole cells has been achieved using a variety of nanosensors: carbon dots,[205,206] organic dyes,[207] fluorescent polymers,[208] and silver nanoclusters.[209] A common defining feature of these sensors is their extremely small size (approximately nm). They can disperse uniformly throughout the cells, and thus enable the mapping of intracellular temperature and the monitoring of temperature-driven metabolic activities. However, it should be noted that the measurement of intracellular temperatures is a nontrivial undertaking and there are still inconsistencies between calculations and measurements,[210–212] which calls for the careful design of any future experiment in this direction.

In the context of cellular-scale thermometry, the results of Tsuji et al.[208] are representative of the achievements of the field. Tsuji and collaborators recently investigated the thermogenesis of brown adipocytes. These are fat cells that possess a large number of mitochondria and carry out the function of maintaining body temperature by heat production. The direct measurement of heat production at the single-cell level, was achieved by employing fluorescent polymers—consisting

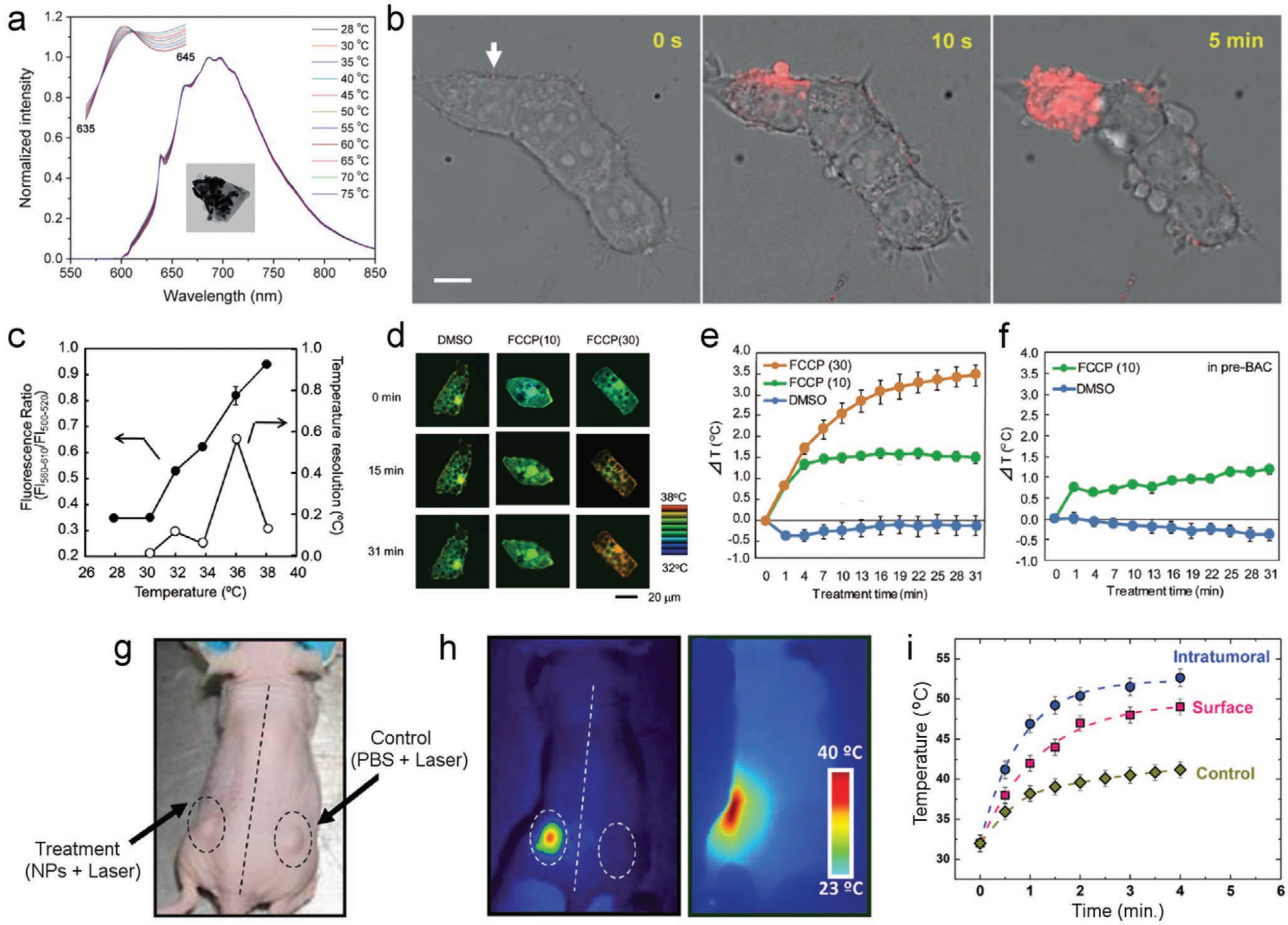

Figure 6. Nanoscale thermometry: bioapplications. a,b) All-optical diamond NV-based nanothermometry: a) temperature-dependent fluorescence spectra of 100 nm fluorescent nanodiamond (FNDs) illuminated by a 594 nm laser in solution. Inset, top-left: enlarged view of the temperature-induced shift of the ZPLs for spectra acquired at 28–75 °C. Inset, bottom: TEM image of a typical FND decorated with citratecapped gold nanorods (GNR). b) Merged bright-field/fluorescence images of an HEK293T cell cluster with GNR-FNDs attached to the plasma membrane after exposure to the 594 nm laser in the presence of PI (45 mm) at different time points. Intracellular PI was observed almost immediately after laser irradiation of the particle indicated by the white arrow. Scale bar: 10 µm. c–f) Intracellular temperature imaging analysis in brown adipose cells (BACs) and pre-BACs in response to uncoupler stimuli using the intracellular cationic fluorescent polymeric thermometer R-CFPT. c) Fluorescence response and temperature resolution of R-CFPT in a BAC extract under microscopy observation. d) Pseudocolor confocal images of the fluorescence ratio (Em. 560–610 nm/Em. 500–520 nm) in R-CFPT-incorporated matured BACs at 15 and 31 min after 10×10^{-6} or 30×10^{-6} м carbonyl cyanide *p*-trifluoromethoxyphenylhydrazone (FCCP) treatment. The scale bar is 20 µm. e) Intracellular temperature change during stimulation of matured BACs with FCCP ($n = 8$, 9, or 9 cells for 0.1% dimethylsulfoxide (DMSO), 10×10^{-6} м FCCP, or 30×10^{-6} м FCCP, respectively). f) Intracellular temperature change during stimulation of pre-BACs with FCCP ($n = 7$ or 16 cells for 0.1% DMSO or 10×10^{-6} м FCCP, respectively). g) Optical image of a mouse with two tumors. A solution of Nd:LaF3 NPs was injected in the left-side tumor whereas the right-side one was used as a control. h) Infrared fluorescence (left) and thermal (right) images of the mouse under 808 nm (4 W cm^{-2}) laser irradiation. The images show the fluorescent and heating signals differentially emitted by the treated tumor. i) Time evolution of the temperature at the tumor surface obtained from the infrared thermal images and from the subtissue fluorescence. a,b) Reproduced with permission.[199] Copyright 2017, Wiley-VCH. c–f) Reproduced with permission.[208] Copyright 2017, Springer Nature. g–i) Reproduced with permission.[213] Copyright 2014, Wiley-VCH.

of a thermosensitive unit, a cationic unit, and two fluorescent units–as nanothermometers. The polymers were passively incorporated into the fat cells for the detection of heat production following the treatment with carbonyl cyanide *p*-trifluoromethoxyphenylhydrazone, which is an uncoupling agent known to accelerate thermogenesis in mitochondria. The researchers observed an increase from 30 to (34.4 ± 0.2) °C of the intracellular temperature upon treatment. They also reported that the increase is significantly higher in matured brown adipocytes than in their precursor cells, which goes from 30 to (32.3±0.2) °C (Figure 6c–f). Further studies with agonist stimulation provided additional proof that the temperature rise is due to endogenous thermogenesis rather than to global heating of the culture medium.

4.1.3. Tissue Thermometry

The first demonstration of tissue thermometry was performed using the temperature-dependent fluorescence signal of green fluorescent proteins (cf. Section 3.1) in *Caenorhabditis elegans*, a nematode commonly found in soil.[83] The nematode is 100 µm in diameter and 1 mm in length; it is transparent, and can be easily imaged by confocal fluorescence microscopy using green fluorescent proteins as biomarkers. Scaling up in size is however nontrivial. Extending the study to small animals like mice inevitably runs into the limit imposed by the short penetration depth of light through tissue. Even for far-red light, i.e., wavelengths >800 nm, the penetration depth is only ≈1 mm. A possible avenue to overcome this hurdle is to expand the thermometric detection range to the short-wave infrared region (i.e., BW-II). Rare-earth-doped nanoparticles are advantageous in this regard as their excitation can be spectrally optimized via doping with various metal ions in different matrices, making them effective nanosensor candidates for thermosensing applications in biological tissues.[213–219]

A main drive for the development of in vivo thermometry techniques is the promise of selective and controlled heating, e.g., for hyperthermia applications. Current methods are magnetic- and optic-based heat treatments, which are often limited in resolution. With the availability of subtissue or even intratumoral temperature readings, precise and efficient control of the thermal treatment by image-guided therapy is achievable. An illustration of this method was given by Carrasco et al.[213] who used highly Nd^{3+}-doped LaF_3 nanocrystals as multifunctional probes to treat breast cancer tumors xenografted on nude mice (Figure 6g–i). These nanoparticles, containing up to 5.6 at% Nd^{3+} ions, can be used for tumor localization, temperature sensing, as well as photothermal heating when exposed to 808 nm light. The research team demonstrated the feasibility of this approach by monitoring the temperature of the tumor surface with an infrared camera, determining the intratumoral temperature through the analysis of subtissue fluorescence derived from the injected LaF_3:Nd^{3+} particles.

4.2. Other Applications

While thermosensing in biological systems is the major driving force of (optical) nanothermometry, nanoscale temperature measurements find applications in other fields.

4.2.1. Microfluidic and Surfaces

Measuring temperatures within microfluidic channels is important for variety of applications, including, for example, understanding solid-liquid interfaces. We presented some representative examples in Section 3.1 when discussing organic dyes (Figure 2c). Effort has also been dedicated to measure temperature with ultrasmall volumes, down to hundreds of picolitres.[220] In general, measuring the temperature within a microfluidic channel is done effectively using temperature-sensitive fluorescent nanoparticles such as the fluorescent dyes (cf. Section 3.1)[29,53,54] and UCNPs (cf. Section 3.3)[221] discussed in this review. Nonoptical methods do also exist, where the microfluidic channel can be printed on-top of a dedicated chips with known temperature gradients.[222

4.2.2. Nanoelectronics and Nanophotonics

High-power nanoelectronics and nanophotonics are fields where monitoring and controlling temperature at the nanoscale is crucial both for performance optimization and prevention of operation failure. In this context, nanothermometers based on diamond color centers (cf. Section 3.4) or other semiconductors such as 2D materials[223] have the potential to advance the field, as these nanothermometers can sustain temperature as high as several hundreds of degrees.

Furthermore, electronic and photonic devices made from (stacks of) 2D materials are growing in scope due to their unique properties.[224,225] Measuring temperature across nanoscale transistors—for instance fabricated from single carbon nanotubes or atomically thin 2D systems—could be realized using the materials themselves as the sensor. This stems from many of these materials being optically active by nature, and thus exploitable for temperature measurement using, for instance, ratiometric anti-Stokes/Stokes photoluminescence measurements.[23] Remote optical thermometry can also be beneficial to measure precise temperature of phase change materials and magnetic materials, especially thin films. One of the main challenges though is the simultaneous and independent measurement of the temperature of these devices and of their magnetic and/or electrical properties.

4.2.3. Microscopy

Another application where remote nanoscale optical thermometry could be useful is during imaging in electron microscopes. Nanostructures are known to heat up during imaging by electron beams and measuring precisely their temperature is currently impossible. However, new technological advancements demonstrated the possibility to measure temperatures by putting optical fibers and other collection optics in situ,[226] as well as by using emitters within the imaged material themselves or from fluorescent particles dispersed on the sample. Drawing from this, similar techniques can be adapted to measure temperature of growing semiconductors or materials—for instance growth of diamond containing color centers. Diamond growth can occur at temperatures of just a few hundred degrees,[227] which is still below the minimum temperature a commercial optical pyrometer can measure. Remote optical thermometry utilizing the embedded color centers could provide precise and accurate temperature at the crystal facet and aid in understanding the growth dynamics of nanodiamond.

5. Conclusions and Outlook

In this review, we have presented an in-depth discussion of the fundamental physicochemical mechanisms at the basis of several nanoscale optical thermometry techniques. The intent was to highlight their intrinsic and absolute capabilities as well as their limitations within a well-defined benchmarking framework, and to critically discuss their use in existing and advanced technological realizations.

5.1. Practical Challenges

Nanoscale optical thermometry is a remarkably well-established field with a vast range and diversity of applications. It is perhaps quite surprising that these techniques have not found a much wider diffusion into real-world, commercial devices. A critical bottleneck is the mass production of the temperature-sensitive nanosensors. While UCNPs and nanodiamonds can be mass produced through several synthesis processes, their optical properties may vary from batch to batch and from particle to particle. This is problematic as it requires calibration of the nanosensors prior to any practical use. Further research in material science is therefore needed to realize more reliable and flexible nanothermometers. However, material science research should not merely revolve around the development of nanothermometers with wider spectral and temperature operation ranges, higher brightness and enhanced sensitivities. Focus should be put onto designing strategies to mitigate the issue of thermal equivalent noise, which hinder the reliable use of nanothermometers in practical applications.

In parallel, as much research and development should be invested in improving the detection systems. Widefield epifluorescence and confocal microscopes are still the predominant types of detection systems used for imaging and for optical temperature-sensing. They are cumbersome and inherently limited in scope and scale. Methods relying on simpler excitation sources (e.g., LEDs) and cheaper detectors (e.g., CCD cameras) would be desirable to address these limitations. Alternatively, one can envision (cf. Section 5.2 below) better detection schemes to overcome the diffraction limit (≥200 nm), which is still setting the spatial resolution of many nanothermometry techniques, despite the nanosensors being only a few nm in size.

5.2. Perspectives and Future Directions

Besides sensing, it would be desirable for nanoscale thermometers to advance from being mere detectors to become actuators. For example in biomedicine, rather than simply monitoring the temperature, the fluorescent nanoparticles could be functionalized with specific surface groups/analytes, which would be released upon reaching a specific temperature—either passively (e.g., via a thermochemical process) or actively (e.g., via a second laser beam). This is not beyond reach given the current state of the art of the techniques developed to functionalize the surface of nanoparticles.

Active thermocontrol of nanoelectronic devices is also an intriguing avenue. A possible scenario is one whereby, if a specific critical temperature is reached on a device, the affected subcircuit is turned off and operation is passively/actively diverted to other subcircuits to maintain the overall functionality of the device.

Nanoscale thermometry beyond the diffraction limit should become routine. Super-resolution imaging has been achieved with most of the fluorophores discussed in this review; optimizing the experiments to detect temperature variation within a sub-100 nm range should be feasible. This is particularly relevant owing to the emergence of 2D material-based devices, where heating occurs at the scale of just a few atomic layers.

Temporal resolution is almost as important as spatial resolution—yet is rarely discussed. Many thermometry techniques are benchmarked based on sensitivity; but resolution is equally important as it carries information about how fast a temperature reading can be for a target resolution. Given the fundamental limit set by thermodynamics on the concept of temperature and by the noise floor due to thermal fluctuations,[24] nanothermometers could be improved to reach realistic temporal resolution approximately µs, which is fast enough for most applications involving rapid temperature transients.[228

Nanoscale spatial resolution and microsecond temporal resolution are key factors for advanced realizations. The most obvious are in biology and in high-power electronics.

In biology, temperature and temperature gradients dictate the behavior of cells, as thermal variations are either the result of cell activities or the response to external stimuli. For instance, cell division, gene expression, enzyme reactions, as well as nominal and pathological (e.g., cancer) cell metabolism occur at specific temperatures or are accompanied by characteristic temperature changes.[4,229,230] The ability to monitor temperature with high spatial (approximately nm) and temporal (approximately µs) resolution becomes therefore an important tool to understand specific biochemical processes and ideally design target-specific diagnostic and therapeutic strategies, including hyperthermia and immunotherapy.[5,6,231,232]

In electronics, devices are reaching sub-micrometric scales and are operating at regimes where high temperature hotspots can form,[233] incurring in performance deterioration or catastrophic failure. The development of nanothermometers with the spatial and temporal resolutions capable of monitoring these regimes has an obvious, practical motivation: to drive the design of devices performing at the cusp between top performance and critical failure. Furthermore, optoelectronic devices made from (stacks of heterogeneous) 2D materials are currently emerging as the most studied materials in condensed matter physics and materials science.[224] The ability to measure local temperatures with resolution down to just a few atomic layers is an intriguing possibility for these novel materials and is accompanied by a fundamental drive: to explore the complex thermal dynamics at play when systems are miniaturized and become quasi-2D.

The last two decades have seen the rise of many promising proof-of-principle demonstrations in optical nanothermometry, where the focus has been mostly on understanding the fundamental mechanisms. The goal of the coming decade should be a technology-oriented one: to harness this fundamental knowledge toward the realization of practical and novel devices.

Acknowledgements

The Australian Research Council (via DP180100077, DP190101058, and DE180100810) are gratefully acknowledged.

Conflict of Interest

The authors declare no conflict of interest.

Keywords

all-optical thermosensors, fluorescent nanoparticles, nanoscale thermometry

Received: February 2, 2020
Revised: March 15, 2020

---

[1] Y. Yue, X. Wang, *Nano Rev.* **2012**, *3*, 11586.
[2] Y. Kamei, M. Suzuki, K. Watanabe, K. Fujimori, T. Kawasaki, T. Deguchi, Y. Yoneda, T. Todo, S. Takagi, T. Funatsu, S. Yuba, *Nat. Methods* **2009**, *6*, 79.
[3] S. V Kumar, P. A. Wigge, *Cell* **2010**, *140*, 136.
[4] T. D. Vreugdenburg, C. D. Willis, L. Mundy, J. E. Hiller, *Breast Cancer Res. Treat.* **2013**, *137*, 665.
[5] A. Schroeder, D. A. Heller, M. M. Winslow, J. E. Dahlman, G. W. Pratt, R. Langer, T. Jacks, D. G. Anderson, *Nat. Rev. Cancer* **2012**, *12*, 39.
[6] D. P O'Neal, L. R. Hirsch, N. J. Halas, J. D Payne, J. L. West, *Cancer Lett.* **2004**, *209*, 171.
[7] C. D. S. Brites, P. P. Lima, N. J. O. Silva, A. Millán, V. S. Amaral, F. Palacio, L. S. D. Carlos, *Nanoscale* **2012**, *4*, 4799.
[8] D. Jaque, F. Vetrone, *Nanoscale* **2012**, *4*, 4301.
[9] M. Quintanilla, L. M. Liz-Marzán, *Nano Today* **2018**, *19*, 126.
[10] T. Bai, N. Gu, *Small* **2016**, *12*, 4590.
[11] B. del Rosal, E. Ximendes, U. Rocha, D. Jaque, *Adv. Opt. Mater.* **2017**, *5*, 1600508.
[12] J. P. Kauppinen, K. T. Loberg, A. J. Manninen, J. P. Pekola, R. A. Voutilainen, *Rev. Sci. Instrum.* **1998**, *69*, 4166.
[13] L. G. Rubin, *Cryogenics* **1997**, *37*, 341.
[14] H. Preston-Thomas, *Metrologia* **1990**, *27*, 3.
[15] M. Hartmann, *Contemp. Phys.* **2006**, *47*, 89.
[16] M. Hartmann, G. Mahler, O. Hess, *Phys. Rev. Lett.* **2004**, *93*, 080402.
[17] K. M. Hoogeboom-Pot, J. N. Hernandez-Charpak, X. Gu, T. D. Frazer, E. H. Anderson, W. Chao, R. W. Falcone, R. Yang, M. M. Murnane, H. C. Kapteyn, D. Nardi, *Proc. Natl. Acad. Sci. USA* **2015**, *112*, 4846.
[18] M. I. Flik, B. I. Choi, K. E. Goodson, *J. Heat Transfer* **1992**, *114*, 666.
[19] G. Chen, *J. Heat Transfer* **1996**, *118*, 539.
[20] K. Esfarjani, G. Chen, H. T. Stokes, *Phys. Rev. B* **2011**, *84*, 085204.
[21] P. Neumann, I. Jakobi, F. Dolde, C. Burk, R. Reuter, G. Waldherr, J. Honert, T. Wolf, A. Brunner, J. H. Shim, D. Suter, H. Sumiya, J. Isoya, J. Wrachtrup, *Nano Lett.* **2013**, *13*, 2738.
[22] G. Kucsko, P. C. Maurer, N. Y. Yao, M. Kubo, H. J. Noh, P. K. Lo, H. Park, M. D. Lukin, *Nature* **2013**, *500*, 54.
[23] T. T. Tran, B. Regan, E. A. Ekimov, Z. Mu, Yu Zhou, W.-Bo Gao, P. Narang, A. S. Solntsev, M. Toth, I. Aharonovich, C. Bradac, *Sci. Adv.* **2019**, *5*, eaav9180.
[24] S. Choi, V. N. Agafonov, V. A. Davydov, T. Plakhotnik, *ACS Photonics* **2019**, *6*, 1387.
[25] L.-A. Labrador-Páez, M. Pedroni, A. Speghini, J. García-Solé, P. Haro-González, D. Jaque, *Nanoscale* **2018**, *10*, 22319.
[26] P. Saccomandi, E. Schena, S. Silvestri, *Int. J. Hyperthermia* **2013**, *29*, 609.
[27] M. E. Köse, B. F. Carroll, K. S. Schanze, *Langmuir* **2005**, *21*, 9121.
[28] K. B. Migler, A. J. Bur, *Polym. Eng. Sci.* **1998**, *38*, 213.
[29] D. Ross, M. Gaitan, L. E. Locascio, *Anal. Chem.* **2001**, *73*, 4117.
[30] G. Baffou, M. P. Kreuzer, F. Kulzer, R. Quidant, *Opt. Express* **2009**, *17*, 3291.
[31] J. Feng, K. Tian, D. Hu, S. Wang, S. Li, Yi Zeng, Yi Li, G. Yang, *Angew. Chem., Int. Ed.* **2011**, *50*, 8072.
[32] S. Li, K. Zhang, J.-M. Yang, L. Lin, H. Yang, *Nano Lett.* **2007**, *7*, 3102.
[33] G. W. Walker, V. C. Sundar, C. M. Rudzinski, A. W. Wun, M. G. Bawendi, D. G. Nocera, *Appl. Phys. Lett.* **2003**, *83*, 3555.
[34] P. Jorge, M. Martins, T. Trindade, J. Santos, F. Farahi, *Sensors* **2007**, *7*, 3489.
[35] V. A. Vlaskin, N. Janssen, J. van Rijssel, R. Beaulac, D. R. Gamelin, *Nano Lett.* **2010**, *10*, 3670.
[36] P. Haro-González, L. Martínez-Maestro, I. R. Martín, J. García-Solé, D. Jaque, *Small* **2012**, *8*, 2652.
[37] N.-N. Dong, M. Pedroni, F. Piccinelli, G. Conti, A. Sbarbati, J. E. Ramírez-Hernández, L. M. Maestro, M. C. Iglesias-de la Cruz, F. Sanz-Rodriguez, A. Juarranz, F. Chen, F. Vetrone, J. A. Capobianco, J. G. Solé, M. Bettinelli, D. Jaque, A. Speghini, *ACS Nano* **2011**, *5*, 8665.
[38] F. Vetrone, R. Naccache, A. Zamarrón, A. Juarranz de la Fuente, F. Sanz-Rodríguez, L. Martinez Maestro, E. Martín Rodriguez, D. Jaque, J. García Solé, J. A. Capobianco, *ACS Nano* **2010**, *4*, 3254.
[39] X. Zhu, W. Feng, J. Chang, Y.-W. Tan, J. Li, M. Chen, Y. Sun, F. Li, *Nat. Commun.* **2016**, *7*, 10437.
[40] X. Wang, X. Kong, Yi Yu, Y. Sun, H. Zhang, *J. Phys. Chem. C* **2007**, *111*, 15119.
[41] K. Green, K. Huang, H. Pan, G. Han, S. F. Lim, *Front. Chem.* **2018**, *6*,416.
[42] M. L. Debasu, D. Ananias, I. Pastoriza-Santos, L. M. Liz-Marzán, J. Rocha, L. S. D. Carlos, *Adv. Mater.* **2013**, *25*, 4817.
[43] T. Plakhotnik, H. Aman, H.-C. Chang, *Nanotechnology* **2015**, *26*, 245501.
[44] J.-W. Fan, I. Cojocaru, J. Becker, I. V. Fedotov, M. H. A. Alkahtani, A. Alajlan, S. Blakley, M. Rezaee, A. Lyamkina, Y. N. Palyanov, Y. M. Borzdov, Y.-P. Yang, A. Zheltikov, P. Hemmer, A. V. Akimov, *ACS Photonics* **2018**, *5*, 765.
[45] C. T. Nguyen, R. E. Evans, A. Sipahigil, M. K. Bhaskar, D. D. Sukachev, V. N. Agafonov, V. A. Davydov, L. F. Kulikova, F. Jelezko, M. D. Lukin, *Appl. Phys. Lett.* **2018**, *112*, 203102.
[46] M. Alkahtani, I. Cojocaru, X. Liu, T. Herzig, J. Meijer, J. Küpper, T. Lühmann, A. V. Akimov, P. R. Hemmer, *Appl. Phys. Lett.* **2018**, *112*, 241902.
[47] J. Kavandi, J. Callis, M. Gouterman, G. Khalil, D. Wright, E. Green, D. Burns, B. McLachlan, *Rev. Sci. Instrum.* **1990**, *61*, 3340.
[48] J. Gallery, M. Gouterman, J. Callis, G. Khalil, B. McLachlan, J. Bell, *Rev. Sci. Instrum.* **1994**, *65*, 712.
[49] T. Liu, B. T. Campbell, S. P. Burns, J. P. Sullivan, *Appl. Mech. Rev.* **1997**, *50*, 227.
[50] M. L. Bhaumik, C. L. Telk, *J. Opt. Soc. Am.* **1964**, *54*, 1211.
[51] H. Szmacinski, J. R. Lakowicz, *Sens. Actuators, B* **1995**, *29*, 16.
[52] M. A. Woodmansee, J. C. Dutton, *Exp. Fluids* **1998**, *24*, 163.
[53] J. Marschewski, R. Brechbühler, S. Jung, P. Ruch, B. Michel, D. Poulikakos, *Int. J. Heat Mass Transfer* **2016**, *95*, 755.
[54] W. M. Abed, A. F. Domingues, R. J. Poole, D. J. C. Dennis, *Int. J. Therm. Sci.* **2017**, *121*, 249.
[55] V. M. Chauhan, R. H. Hopper, S. Z. Ali, E. M. King, F. Udrea, C. H. Oxley, J. W. Aylott, *Sens. Actuators, B* **2014**, *192*, 126.
[56] R. Samy, T. Glawdel, C. L. Ren, *Anal. Chem.* **2008**, *80*, 369.
[57] S. Arai, S.-C. Lee, D. Zhai, M. Suzuki, Y. T. Chang, *Sci. Rep.* **2015**, *4*, 6701.
[58] H. Itoh, S. Arai, T. Sudhaharan, S.-C. Lee, Y.-T. Chang, S. Ishiwata, M. Suzuki, E. B Lane, *Chem. Commun.* **2016**, *52*, 4458.
[59] C. F. Chapman, Y. Liu, G. J. Sonek, B. J. Tromberg, *Photochem. Photobiol.* **1995**, *62*, 416.
[60] S. Arai, M. Suzuki, S.-J. Park, J. S. Yoo, Lu Wang, N. Kang, H.-Ho Ha, Y.-T. Chang, *Chem. Commun.* **2015**, *51*, 8044.
[61] M. Homma, Y. Takei, A. Murata, T. Inoue, S. Takeoka, *Chem. Commun.* **2015**, *51*, 6194.
[62] C. Klein, R. H. Engler, U. Henne, W. E. Sachs, *Exp. Fluids* **2005**, *39*, 475.

[63] D.-A. Mendels, E. M. Graham, S. W. Magennis, A. C. Jones, F. Mendels, *Microfluid. Nanofluid.* **2008**, *5*, 603.
[64] T. Karstens, K. Kobs, *J. Phys. Chem.* **1980**, *84*, 1871.
[65] J. J. Shah, M. Gaitan, J. Geist, *Anal. Chem.* **2009**, *81*, 8260.
[66] M. A. Bennet, P. R. Richardson, J. Arlt, A. McCarthy, G. S. Buller, A. C. Jones, *Lab Chip* **2011**, *11*, 3821.
[67] K. A. Zachariasse, G. Duveneck, R. Busse, *J. Am. Chem. Soc.* **1984**, *106*, 1045.
[68] A. J. Bur, M. G. Vangel, S. C. Roth, *Polym. Eng. Sci.* **2001**, *41*, 1380.
[69] D. P Jing, L. Bokobza, P. Sergot, L. Monnerie, P. Collart, F. C De Schryver, *Polymer* **1989**, *30*, 443.
[70] B. D. Freeman, L. Bokobza, P. Sergot, L. Monnerie, F. C. De Schryver, *J. Lumin.* **1991**, *48-49*, 259.
[71] M. T Albelda, E. García-España, L. Gil, J. C. Lima, C. Lodeiro, J. Seixas de Melo, M. J. Melo, A. J Parola, F. Pina, C. Soriano, *J. Phys. Chem. B* **2003**, *107*, 6573.
[72] N. Chandrasekharan, L. A. Kelly, *J. Am. Chem. Soc.* **2001**, *123*, 9898.
[73] V. V. Volchkov, B. M. Uzhinov, *High Energy Chem.* **2008**, *42*, 153.
[74] J. Feng, L. Xiong, S. Wang, S. Li, Yi Li, G. Yang, *Adv. Funct. Mater.* **2013**, *23*, 340.
[75] K. Rotkiewicz, K. H. Grellmann, Z. R. Grabowski, *Chem. Phys. Lett.* **1973**, *19*, 315.
[76] O. Kahn, *Curr. Opin. Solid State Mater. Sci.* **1996**, *1*, 547.
[77] W. Nicolazzi, A. Bousseksou, *C. R. Chim.* **2018**, *21*, 1060.
[78] A. Tokarev, L. Salmon, Y. Guari, W. Nicolazzi, G. Molnár, A. Bousseksou, *Chem. Commun.* **2010**, *46*, 8011.
[79] L. Salmon, G. Molnár, D. Zitouni, C. Quintero, C. Bergaud, J.-C. Micheau, A. Bousseksou, *J. Mater. Chem.* **2010**, *20*, 5499.
[80] M. Engeser, L. Fabbrizzi, M. Licchelli, D. Sacchi, *Chem. Commun.* **1999**, 1191.
[81] A. Kawski, *Crit. Rev. Anal. Chem.* **1993**, *23*, 459.
[82] J. S. Donner, S. A. Thompson, M. P. Kreuzer, G. Baffou, R. Quidant, *Nano Lett.* **2012**, *12*, 2107.
[83] J. S. Donner, S. A. Thompson, C. Alonso-Ortega, J. Morales, L. G. Rico, S. I. C. O Santos, R. Quidant, *ACS Nano* **2013**, *7*, 8666.
[84] J. Sakakibara, R. J. Adrian, *Exp. Fluids* **1999**, *26*, 7.
[85] S. Arai, F. Ferdinandus, S. Takeoka, S. Ishiwata, H. Sato, M. Suzuki, *Analyst* **2015**, *140*, 7534.
[86] U. Resch-Genger, M. Grabolle, S. Cavaliere-Jaricot, R. Nitschke, T. Nann, *Nat. Methods* **2008**, *5*, 763.
[87] M. BruchezJr., *Science* **1998**, *281*, 2013.
[88] W. C. Chan, *Science* **1998**, *281*, 2016.
[89] I. L. Medintz, H. T Uyeda, E. R. Goldman, H. Mattoussi, *Nat. Mater.* **2005**, *4*, 435.
[90] B. O. Dabbousi, J. Rodriguez-Viejo, F. V. Mikulec, J. R. Heine, H. Mattoussi, R. Ober, K. F. Jensen, M. G. Bawendi, *J. Phys. Chem. B* **1997**, *101*, 9463.
[91] M. A. Hines, P. Guyot-Sionnest, *J. Phys. Chem.* **1996**, *100*, 468.
[92] A. Olkhovets, R.-C. Hsu, A. Lipovskii, F. W. Wise, *Phys. Rev. Lett.* **1998**, *81*, 3539.
[93] F. W. Wise, *Acc. Chem. Res.* **2000**, *33*, 773.
[94] A. Narayanaswamy, L. F. Feiner, A. Meijerink, P. J. van der Zaag, *ACS Nano* **2009**, *3*, 2539.
[95] D. Zhou, M. Lin, X. Liu, J. Li, Z. Chen, D. Yao, H. Sun, H. Zhang, B. Yang, *ACS Nano* **2013**, *7*, 2273.
[96] Y. P. Varshni, *Physica* **1967**, *34*, 149.
[97] K. P. O'Donnell, X. Chen, *Appl. Phys. Lett.* **1991**, *58*, 2924.
[98] P. B. Allen, M. Cardona, *Phys. Rev. B* **1983**, *27*, 4760.
[99] G. Scamarcio, M. Lugará, D. Manno, *Phys. Rev. B* **1992**, *45*, 13792.
[100] S. Nomura, T. Kobayashi, *Phys. Rev. B* **1992**, *45*, 1305.
[101] H. Y. Fan, *Phys. Rev.* **1951**, *82*, 900.
[102] C. Keffer, T. M. Hayes, A. Bienenstock, *Phys. Rev. B* **1970**, *2*, 1966.
[103] T. Takagahara, *Phys. Rev. Lett.* **1993**, *71*, 3577.
[104] O. I. Mićić, H. M. Cheong, H. Fu, A. Zunger, J. R. Sprague, A. Mascarenhas, A. J. Nozik, *J. Phys. Chem. B* **1997**, *101*, 4904.
[105] S. Rudin, T. L. Reinecke, B. Segall, *Phys. Rev. B* **1990**, *42*, 11218.
[106] D. Valerini, A. Cretí, M. Lomascolo, L. Manna, R. Cingolani, M. Anni, *Phys. Rev. B* **2005**, *71*, 235409.
[107] A. Al Salman, A. Tortschanoff, M. B. Mohamed, D. Tonti, F. van Mourik, M. Chergui, *Appl. Phys. Lett.* **2007**, *90*, 093104.
[108] T. Takagahara, *J. Lumin.* **1996**, *70*, 129.
[109] B. Han, W. L. Hanson, K. Bensalah, A. Tuncel, J. M. Stern, J. A. Cadeddu, *Ann. Biomed. Eng.* **2009**, *37*, 1230.
[110] S. Wang, S. Westcott, W. Chen, *J. Phys. Chem. B* **2002**, *106*, 11203.
[111] M. D. Leistikow, J. Johansen, A. J. Kettelarij, P. Lodahl, W. L. Vos, *Phys. Rev. B* **2009**, *79*, 045301.
[112] G. Schlegel, J. Bohnenberger, I. Potapova, A. Mews, *Phys. Rev. Lett.* **2002**, *88*, 137401.
[113] A. M. Kapitonov, A. P. Stupak, S. V. Gaponenko, E. P. Petrov, A. L. Rogach, A. Eychmüller, *J. Phys. Chem. B* **1999**, *103*, 10109.
[114] C. de Mello Donegá, M. Bode, A. Meijerink, *Phys. Rev. B* **2006**, *74*, 085320.
[115] Q. Dai, Yu Zhang, Y. Wang, M. Z. Hu, Bo Zou, Y. Wang, W. W. Yu, *Langmuir* **2010**, *26*, 11435.
[116] R. Beaulac, P. I. Archer, J. van Rijssel, A. Meijerink, D. R. Gamelin, *Nano Lett.* **2008**, *8*, 2949.
[117] L. M. Maestro, E. M. Rodríguez, F. S. Rodríguez, M. C. Iglesias-de la Cruz, A. Juarranz, R. Naccache, F. Vetrone, D. Jaque, J. A. Capobianco, J. G. Solé, *Nano Lett.* **2010**, *10*, 5109.
[118] L. M. Maestro, C. Jacinto, U. R. Silva, F. Vetrone, J. A. Capobianco, D. Jaque, J. G. Solé, *Small* **2011**, *7*, 1774.
[119] J. M. Lupton, *Appl. Phys. Lett.* **2002**, *81*, 2478.
[120] Y. Fan, H. Liu, R. Han, Lu Huang, H. Shi, Y. Sha, Y. Jiang, *Sci. Rep.* **2015**, *5*, 9908.
[121] Y. Nonoguchi, T. Nakashima, T. Kawai, *J. Phys. Chem. C* **2007**, *111*, 11811.
[122] G. Hong, J. T. Robinson, Y. Zhang, S. Diao, A. L. Antaris, Q. Wang, H. Dai, *Angew. Chem., Int. Ed.* **2012**, *51*, 9818.
[123] C. Li, F. Li, Y. Zhang, W. Zhang, X.-E. Zhang, Q. Wang, *ACS Nano* **2015**, *9*, 12255.
[124] G. Chen, Y. Zhang, C. Li, D. Huang, Q. Wang, Q. Wang, *Adv. Healthcare Mater.* **2018**, *7*, 1800497.
[125] D. R. Larson, *Science* **2003**, *300*, 1434.
[126] Cao, U. Banin, *J. Am. Chem. Soc.* **2000**, *122*, 9692.
[127] H. Liu, Y. Fan, J. Wang, Z. Song, H. Shi, R. Han, Y. Sha, Y. Jiang, *Sci. Rep.* **2015**, *5*, 14879.
[128] K. M. Tsoi, Q. Dai, B. A. Alman, W. C. W. Chan, *Acc. Chem. Res.* **2013**, *46*, 662.
[129] K. M. McCabe, M. Hernandez, *Pediatr. Res.* **2010**, *67*, 469.
[130] S. S. Laha, A. R. Naik, E. R. Kuhn, M. Alvarez, A. Sujkowski, R. J. Wessells, B. P. Jena, *Nano Lett.* **2017**, *17*, 1262.
[131] J.-M. Yang, H. Yang, L. Lin, *ACS Nano* **2011**, *5*, 5067.
[132] Y. Zhao, C. Riemersma, F. Pietra, R. Koole, C. de Mello Donegá, A. Meijerink, *ACS Nano* **2012**, *6*, 9058.
[133] F. Helmchen, W. Denk, *Nat. Methods* **2005**, *2*, 932.
[134] W. Denk, J. Strickler, W. Webb, *Science* **1990**, *248*, 73.
[135] R. Naccache, F. Vetrone, A. Speghini, M. Bettinelli, J. A. Capobianco, *J. Phys. Chem. C* **2008**, *112*, 7750.
[136] A. Priyam, N. M. Idris, Y. Zhang, *J. Mater. Chem.* **2012**, *22*, 960.
[137] F. Wang, Yu Han, C. S. Lim, Y. Lu, J. Wang, J. Xu, H. Chen, C. Zhang, M. Hong, X. Liu, *Nature* **2010**, *463*, 1061.
[138] F. Auzel, *Chem. Rev.* **2004**, *104*, 139.
[139] C. D. S. Brites, S. Balabhadra, L. D. Carlos, *Adv. Opt. Mater.* **2019**, *7*, 1801239.
[140] C. D. S. Brites, A. Millán, L. D. Carlos, in *Handbook on the Physics and Chemistry of Rare Earths* (Eds: B. Jean-Claude, P. Vitalij K), Vol. 49, Elsevier, Amsterdam **2016**, pp. 339–427.
[141] P. Löw, B. Kim, N. Takama, C. Bergaud, *Small* **2008**, *4*, 908.
[142] S. Wu, G. Han, D. J. Milliron, S. Aloni, V. Altoe, D. V. Talapin, B. E. Cohen, P. J. Schuck, *Proc. Natl. Acad. Sci. USA* **2009**, *106*, 10917.

[143] D. K. Williams, B. Bihari, B. M. Tissue, J. M. McHale, *J. Phys. Chem. B* **1998**, *102*, 916.
[144] F. Vetrone, R. Naccache, A. Juarranz de la Fuente, F. Sanz-Rodríguez, A. Blazquez-Castro, E. M. Rodriguez, D. Jaque, J. G. Solé, J. A. Capobianco, *Nanoscale* **2010**, *2*, 495.
[145] J. Dong, J. I. Zink, *ACS Nano* **2014**, *8*, 5199.
[146] W. Xu, X. Gao, L. Zheng, Z. Zhang, W. Cao, *Sens. Actuators, B* **2012**, *173*, 250.
[147] Q. Lü, Y. Wu, A. Li, Y. Wang, Y. Gao, H. Peng, *Mater. Sci. Eng., B* **2011**, *176*, 1041.
[148] Y. Lei, H. Song, L. Yang, L. Yu, Z. Liu, G. Pan, X. Bai, L. Fan, *J. Chem. Phys.* **2005**, *123*, 174710.
[149] X. Bai, H. Song, G. Pan, Y. Lei, T. Wang, X. Ren, S. Lu, B. Dong, Q. Dai, L. Fan, *J. Phys. Chem. C* **2007**, *111*, 13611.
[150] Ye-Fu Wang, G.-Y. Liu, L.-D. Sun, J.-W. Xiao, J.-C. Zhou, C.-H. Yan, *ACS Nano* **2013**, *7*, 7200.
[151] T. Kushida, H. M. Marcos, J. E. Geusic, *Phys. Rev.* **1968**, *167*, 289.
[152] P. Chen, M. Song, E. Wu, B. Wu, J. Zhou, H. Zeng, X. Liu, J. Qiu, *Nanoscale* **2015**, *7*, 6462.
[153] Ol. A. Savchuk, P. Haro-González, J. J. Carvajal, D. Jaque, J. Massons, M. Aguiló, F. Díaz, *Nanoscale* **2014**, *6*, 9727.
[154] J. Zhang, B. Ji, G. Chen, Z. Hua, *Inorg. Chem.* **2018**, *57*, 5038.
[155] Lu Yao, Y. Li, D. Xu, H. Lin, Y. Peng, S. Yang, Y. Zhang, *New J. Chem.* **2019**, *43*, 3848.
[156] Lu Yao, D. Xu, Y. Li, H. Lin, S. Yang, Y. Zhang, *Appl. Surf. Sci.* **2019**, *466*, 320.
[157] Ol. A. Savchuk, J. J. Carvajal, M. C. Pujol, J. Massons, P. Haro-González, O. Martínez, J. Jiménez, M. Aguiló, F. Díaz, *J. Lumin.* **2016**, *169*, 711.
[158] L. Li, C. Guo, S. Jiang, D. K. Agrawal, T. Li, *RSC Adv.* **2014**, *4*, 6391.
[159] D. J. Gargas, E. M. Chan, A. D. Ostrowski, S. Aloni, M. V. P. Altoe, E. S. Barnard, B. Sanii, J. J. Urban, D. J. Milliron, B. E. Cohen, P. J Schuck, *Nat. Nanotechnol.* **2014**, *9*, 300.
[160] K. K. Green, J. Wirth, S. F. Lim, *Sci. Rep.* **2017**, *7*, 762.
[161] Q. Zhan, J. Qian, H. Liang, G. Somesfalean, D. Wang, S. He, Z. Zhang, S. Andersson-Engels, *ACS Nano* **2011**, *5*, 3744.
[162] P. Jiang, C.-N. Zhu, Z.-L. Zhang, Z.-Q. Tian, D.-W. Pang, *Biomaterials* **2012**, *33*, 5130.
[163] B. del Rosal, E. Carrasco, F. Ren, A. Benayas, F. Vetrone, F. Sanz-Rodríguez, D. Ma, Á. Juarranz, D. Jaque, *Adv. Funct. Mater.* **2016**, *26*, 6060.
[164] M. Pollnau, D. R. Gamelin, S. R. Lüthi, H. U. Güdel, M. P. Hehlen, *Phys. Rev. B* **2000**, *61*, 3337.
[165] N. B. Manson, J. P. Harrison, M. J. Sellars, *Phys. Rev. B* **2006**, *74*, 104303.
[166] C. Bradac, W. Gao, J. Forneris, M. E. Trusheim, I. Aharonovich, *Nat. Commun.* **2019**, *10*, 5625.
[167] G. Balasubramanian, I. Y. Chan, R. Kolesov, M. Al-Hmoud, J. Tisler, C. Shin, C. Kim, A. Wojcik, P. R. Hemmer, A. Krueger, T. Hanke, A. Leitenstorfer, R. Bratschitsch, F. Jelezko, J. Wrachtrup, *Nature* **2008**, *455*, 648.
[168] D. B. Bucher, D. P. L. Aude Craik, M. P. Backlund, M. J. Turner, O. Ben Dor, D. R. Glenn, R. L. Walsworth, *Nat. Protoc.* **2019**, *14*, 2707.
[169] T. Plakhotnik, D. Gruber, *Phys. Chem. Chem. Phys.* **2010**, *12*, 9751.
[170] V. M. Acosta, E. Bauch, M. P. Ledbetter, A. Waxman, L.-S. Bouchard, D. Budker, *Phys. Rev. Lett.* **2010**, *104*, 070801.
[171] G. Davies, *J. Phys. C: Solid State Phys.* **1974**, *7*, 3797.
[172] M. W. Doherty, N. B. Manson, P. Delaney, F. Jelezko, J. Wrachtrup, L. C. L. Hollenberg, *Phys. Rep.* **2013**, *528*, 1.
[173] T. Plakhotnik, M. W. Doherty, J. H. Cole, R. Chapman, N. B. Manson, *Nano Lett.* **2014**, *14*, 4989.
[174] M. W. Doherty, V. M. Acosta, A. Jarmola, M. S. J. Barson, N. B. Manson, D. Budker, L. C. L. Hollenberg, *Phys. Rev. B* **2014**, *90*, 041201.
Q9 [175] D. M. Toyliet al., *Phys. Rev. X* **2012**, *2*, 031001.
[176] X.-D. Chen, C.-H. Dong, F.-W. Sun, C.-L. Zou, J.-M. Cui, Z.-F. Han, G.-C. Guo, *Appl. Phys. Lett.* **2011**, *99*, 161903.
[177] E. Neu, C. Hepp, M. Hauschild, S. Gsell, M. Fischer, H. Sternschulte, D. Steinmüller-Nethl, M. Schreck, C. Becher, *New J. Phys.* **2013**, *15*, 043005.
[178] A. A. Maradudin in *Solid State Physics* (Eds: F. Seitz, D. Turnbull), Vol. *18*, Academic Press, San Diego, CA **1966**, pp. 273–420.
[179] G. Davies, *Rep. Prog. Phys.* **1981**, *44*, 787.
[180] V. Hizhnyakov, H. Kaasik, I. Sildos, *Phys. Status Solidi B* **2002**, *234*, 644.
[181] K.-M. C. Fu, C. Santori, P. E. Barclay, L. J. Rogers, N. B. Manson, R. G. Beausoleil, *Phys. Rev. Lett.* **2009**, *103*, 256404.
[182] V. Hizhnyakov, P. Reineker, *J. Chem. Phys.* **1999**, *111*, 8131.
[183] R. Schirhagl, K. Chang, M. Loretz, C. L. Degen, *Annu. Rev. Phys. Chem.* **2014**, *65*, 83.
[184] M. S. Grinolds, M. Warner, K. De Greve, Y. Dovzhenko, L. Thiel, R. L. Walsworth, S. Hong, P. Maletinsky, A. Yacoby, *Nat. Nanotechnol.* **2014**, *9*, 279.
[185] K. D. Jahnke, A. Sipahigil, J. M. Binder, M. W. Doherty, M. Metsch, L. J. Rogers, N. B. Manson, M. D. Lukin, F. Jelezko, *New J. Phys.* **2015**, *17*, 043011.
[186] I. Aharonovich, E. Neu, *Adv. Opt. Mater.* **2014**, *2*, 911.
[187] J. M. Say, C. van Vreden, D. J. Reilly, L. J. Brown, J. R. Rabeau, N. J. C. King, *Biophys. Rev.* **2011**, *3*, 171.
[188] A. T. M. A. Rahman, A. C. Frangeskou, M. S. Kim, S. Bose, G. W. Morley, P. F. Barker, *Sci. Rep.* **2016**, *6*, 21633.
[189] F. Dolde, H. Fedder, M. W. Doherty, T. Nöbauer, F. Rempp, G. Balasubramanian, T. Wolf, F. Reinhard, L. C. L. Hollenberg, F. Jelezko, J. Wrachtrup, *Nat. Phys.* **2011**, *7*, 459.
[190] R. Gao, S. Zhao, X. Jiang, Y. Sun, S. Zhao, J. Gao, J. Borleis, S. Willard, M. Tang, H. Cai, Y. Kamimura, Y. Huang, J. Jiang, Z. Huang, A. Mogilner, T. Pan, P. N. Devreotes, M. Zhao, *Sci. Signaling* **2015**, *8*, ra50.
[191] H. Zhou, M. Sharma, O. Berezin, D. Zuckerman, M. Y. Berezin, *ChemPhysChem* **2016**, *17*, 27.
[192] M. Nakano, T. Nagai, *J. Photochem. Photobiol., C* **2017**, *30*, 2.
[193] S. Sotoma, C. P. Epperla, H.-C. Chang, *ChemNanoMat* **2018**, *4*, 15.
[194] T.-R. Xie, C.-F. Liu, J.-S. Kang, *Biophys. Rep.* **2017**, *3*, 85.
[195] M. Nakano, Y. Arai, I. Kotera, K. Okabe, Y. Kamei, T. Nagai, *PLoS One* **2017**, *12*, e0172344.
[196] O. A. Savchuk, O. F. Silvestre, R. M. R. Adão, J. B. Nieder, *Sci. Rep.* **2019**, *9*, 7535.
[197] S. Uchiyama, C. Gota, T. Tsuji, N. Inada, *Chem. Commun.* **2017**, *53*, 10976.
[198] P. Rodríguez-Sevilla, Y. Zhang, P. Haro-González, F. Sanz-Rodríguez, F. Jaque, J. G. Solé, X. Liu, D. Jaque, *Adv. Mater.* **2016**, *28*, 2421.
[199] P.-C. Tsai, C. P. Epperla, Jo-S Huang, O. Y. Chen, C.-C. Wu, H.-C. Chang, *Angew. Chem., Int. Ed.* **2017**, *56*, 3025.
[200] M. Alkahtani, L. Jiang, R. Brick, P. Hemmer, M. Scully, *Opt. Lett.* **2017**, *42*, 4812.
[201] D. A. Simpson, E. Morrisroe, J. M. McCoey, A. H. Lombard, D. C. Mendis, F. Treussart, L. T. Hall, S. Petrou, L. C. L. Hollenberg, *ACS Nano* **2017**, *11*, 12077.
[202] T. Sekiguchi, S. Sotoma, Y. Harada, *Biophys. Physicobiol.* **2018**, *15*, 229.
[203] M. H. Alkahtani, F. Alghannam, L. Jiang, A. A. Rampersaud, R. Brick, C. L. Gomes, M. O. Scully, P. R. Hemmer, *Opt. Lett.* **2018**, *43*, 3317.
[204] E. Glushkov, V. Navikas, A. Radenovic, *Chimia* **2019**, *73*, 73.
[205] C. Wang, H. Lin, Z. Xu, Y. Huang, M. G. Humphrey, C. Zhang, H. Lin, Z. Xu, Y. Huang, M. G. Humphrey, C. Zhang, *ACS Appl. Mater. Interfaces* **2016**, *8*, 6621.
[206] S. Kalytchuk, K. Poláková, Yu Wang, J. P. Froning, K. Cepe, A. L. Rogach, R. Zbořil, *ACS Nano* **2017**, *11*, 1432.
[207] M. M. Ogle, A. D. Smith McWilliams, M. J. Ware, S. A. Curley, S. J. Corr, A. A. Martí, *J. Phys. Chem. B* **2019**, *123*, 7282.

[208] T. Tsuji, K. Ikado, H. Koizumi, S. Uchiyama, K. Kajimoto, *Sci. Rep.* **2017**, *7*, 12889.
[209] W. Zhou, J. Zhu, Ye Teng, B. Du, Xu Han, S. Dong, *Nano Res.* **2018**, *11*, 2012.
[210] S. Kiyonaka, R. Sakaguchi, I. Hamachi, T. Morii, T. Yoshizaki, Y. Mori, *Nat. Methods* **2015**, *12*, 801.
[211] M. Suzuki, V. Zeeb, S. Arai, K. Oyama, S. Ishiwata, *Nat. Methods* **2015**, *12*, 802.
[212] G. Baffou, H. Rigneault, D. Marguet, L. Jullien, *Nat. Methods* **2014**, *11*, 899.
[213] E. Carrasco, B. del Rosal, F. Sanz-Rodríguez, Á. J. de la Fuente, P. H. Gonzalez, U. Rocha, K. U. Kumar, C. Jacinto, J. G. Solé, D. Jaque, *Adv. Funct. Mater.* **2015**, *25*, 615.
[214] I. E. Kolesnikov, A. A. Kalinichev, M. A. Kurochkin, E. V. Golyeva, E. Yu. Kolesnikov, A. V. Kurochkin, E. Lähderanta, M. D. Mikhailov, *Sci. Rep.* **2017**, *7*, 18002.
[215] P. Cortelletti, A. Skripka, C. Facciotti, M. Pedroni, G. Caputo, N. Pinna, M. Quintanilla, A. Benayas, F. Vetrone, A. Speghini, *Nanoscale* **2018**, *10*, 2568.
[216] H. Suo, F. Hu, X. Zhao, Z. Zhang, T. Li, C. Duan, M. Yin, C. Guo, *J. Mater. Chem. C* **2017**, *5*, 1501.
[217] I. E. Kolesnikov, A. A. Kalinichev, M. A. Kurochkin, D. V. Mamonova, E. Y. Kolesnikov, E. Lähderanta, M. D. Mikhailov, *Nanotechnology* **2019**, *30*, 145501.
[218] M. Runowski, A. Bartkowiak, M. Majewska, I. R. Martín, S. Lis, *J. Lumin.* **2018**, *201*, 104.
[219] M. Runowski, N. Stopikowska, D. Szeremeta, S. Goderski, M. Skwierczyńskail, S. Lis, *ACS Appl. Mater. Interfaces* **2019**, *11*, 13389.
[220] J. Wu, T. Y. Kwok, X. Li, W. Cao, Yu Wang, J. Huang, Y. Hong, D. Zhang, W. Wen, *Sci. Rep.* **2013**, *3*, 3321.
[221] R. G. Geitenbeek, J. C. Vollenbroek, H. M. H. Weijgertze, C. B. M. Tregouet, A.-E. Nieuwelink, C. L. Kennedy, B. M. Weckhuysen, D. Lohse, A. van Blaaderen, A. van den Berg, M. Odijk, A. Meijerink, *Lab Chip* **2019**, *19*, 1236.
[222] B. A. McKenzie, W. H. Grover, *PLoS One* **2017**, *12*, e0189430.
[223] M. Kianinia, B. Regan, S. A. Tawfik, T. T. Tran, M. J. Ford, I. Aharonovich, M. Toth, *ACS Photonics* **2017**, *4*, 768.
[224] A. K. Geim, I. V. Grigorieva, *Nature* **2013**, *499*, 419.
[225] C. Palacios-Berraquero, M. Barbone, D. M. Kara, X. Chen, I. Goykhman, D. Yoon, A. K. Ott, J. Beitner, K. Watanabe, T. Taniguchi, A. C. Ferrari, M. Atatüre, *Nat. Commun.* **2016**, *7*, 12978.
[226] S. Blakley, X. Liu, I. Fedotov, I. Cojocaru, C. Vincent, M. Alkahtani, J. Becker, M. Kieschnick, T. Lühman, J. Meijer, P. Hemmer, A. Akimov, M. Scully, A. Zheltikov, *ACS Photonics* **2019**, *6*, 1690.
[227] S. Drijkoningen, P. Pobedinskas, S. Korneychuk, A. Momot, Y. Balasubramaniam, M. K. Van Bael, S. Turner, J. Verbeeck, M. Nesládek, K. Haenen, *Cryst. Growth Des.* **2017**, *17*, 4306.
[228] R. B. Simon, J. W. Pomeroy, M. Kuball, *Appl. Phys. Lett.* **2014**, *104*, 213503.
[229] R. Sakaguchi, S. Kiyonaka, Y. Mori, *Curr. Opin. Biotechnol.* **2015**, *31*, 57.
[230] B. B. Lowell, B. M. Spiegelman, *Nature* **2000**, *404*, 652.
[231] J. Z. Zhang, *J. Phys. Chem. Lett.* **2010**, *1*, 686.
[232] A. J. Moy, J. W. Tunnell, *Adv. Drug Delivery Rev.* **2017**, *114*, 175.
[233] F. Menges, P. Mensch, H. Schmid, H. Riel, A. Stemmer, B. Gotsmann, *Nat. Commun.* **2016**, *7*, 10874.

ADVANCED
OPTICAL
MATERIALS

Editorial Office:
Wiley-VCH Verlag
Boschstraße 12, 69469 Weinheim
Germany
Tel.: (+49) 6201 606 235 or 432
Fax: (+49) 6201 606 510

Email: advopticalmat@wiley-vch.de

Reprint Order Form

Manuscript No.: ____________________________________
Customer No.: (if available) __________________________
Purchase Order No.: ____________________________
Author: ______________________________________

Charges for Reprints in Euro (excl. VAT), prices are subject to change. Minimum order 50 copies.

No. of pages	**50** copies	**100** copies	**150** copies	**200** copies	**300** copies	**500** copies
1– 4	345,—	395,—	425,—	445,—	548,—	752,—
5– 8	490,—	573,—	608,—	636,—	784,—	1077,—
9–12	640,—	739,—	786,—	824,—	1016,—	1396,—
13–16	780,—	900,—	958,—	1004,—	1237,—	1701,—
17–20	930,—	1070,—	1138,—	1196,—	1489,—	2022,—
every additional 4 pages	147,—	169,—	175,—	188,—	231,—	315,—

Information regarding VAT: The charges for publication of *cover pictures /reprints/issues/poster/Video abstracts/* are considered to be "supply of services" and therefore subject to German VAT. However, if you are an institutional customer outside Germany, the tax can be waived if you provide us with the valid VAT number of your company. Non-EU customers may have a VAT number starting with "EU" instead of their country code, if they are registered with the EU tax authorities. If you do not have a valid EU VAT number and you are a taxable person doing business in a non-EU country, please provide a certification from your local tax authorities confirming that you are a taxable person under local tax law. Please note that the certification must confirm that you are a taxable person and are conducting an economic activity in your country. **Note:** certifications confirming that you are a tax-exempt legal body (non-profit organization, public body, school, political party, etc.) in your country do not exempt you from paying German VAT.

Please send me send bill me for

☐ no. of reprints

☐ high-resolution PDF file (330 Euro excl. VAT)
E-mail address: ____________________

❖ Special Offer:

If you order 200 or more reprints you will get
a PDF file for half price.

Please note: It is not permitted to present the PDF file on the internet or on company homepages.

Cover Posters (prices excl. VAT)
Posters of published covers are available in two sizes:
☐ DinA2 42 x 60 cm / 17 x 24in (one copy: 39 Euro)

☐ DinA1 60 x 84 cm / 24 x 33in (one copy: 49 Euro)

Postage for shipping (prices excl. VAT)
overseas +25 Euro
within Europe +15 Euro

____
Date, Signature

VAT number: ______________________________

Mail reprints / copies of the issue to:

____
____
____
____
____

Send bill to:

____
____
____
____

☐ **I will pay by bank transfer**

☐ **I will pay by credit card**

VISA, Mastercard and AMERICAN EXPRESS
For your security please use this link (Credit Card Token Generator) to create a secure code Credit Card Token and include this number in the form instead of the credit card data. Click here:
https://www.wiley-vch.de/editorial_production/index.php

CREDIT CARD TOKEN NUMBER

						V									

Wiley-VCH Verlag GmbH & Co. KGaA – A company of John Wiley & Sons, Inc. -
Location of the Company: Weinheim - Trade Register: Mannheim, HRB 432833.
Chairman of the Supervisory Board: John Kritzmacher
General Partner: John Wiley & Sons GmbH, Location: Weinheim –
Trade Register Mannheim, HRB 432296 – Managing Director: Sabine Haag and Dr. Guido Herrmann

WILEY-VCH